Materials Reports: Energy 3 (2023) 100213

Contents lists available at ScienceDirect

Materials Reports: Energy

journal homepage: www.keaipublishing.com/en/journals/materials-reports-energy

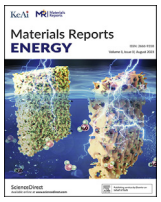

Review

Computational design of promising 2D electrode materials for Li-ion and Li–S battery applications

Ke Fan, Yuen Hong Tsang **, Haitao Huang *

Department of Applied Physics and Research Institute for Smart Energy, The Hong Kong Polytechnic University, Hong Kong, China

ARTICLE INFO

Keywords:
Lithium-ion batteries
Lithium-sulfur batteries
2D electrode materials
Computational design

ABSTRACT

Lithium-ion batteries (LIBs) and lithium-sulfur (Li–S) batteries are two types of energy storage systems with significance in both scientific research and commercialization. Nevertheless, the rational design of electrode materials for overcoming the bottlenecks of LIBs and Li–S batteries (such as low diffusion rates in LIBs and low sulfur utilization in Li–S batteries) remain the greatest challenge, while two-dimensional (2D) electrodes materials provide a solution because of their unique structural and electrochemical properties. In this article, from the perspective of *ab-initio* simulations, we review the design of 2D electrode materials for LIBs and Li–S batteries. We first propose the theoretical design principles for 2D electrodes, including stability, electronic properties, capacity, and ion diffusion descriptors. Next, classified examples of promising 2D electrodes designed by theoretical simulations are given, covering graphene, phosphorene, MXene, transition metal sulfides, and so on. Finally, common challenges and a future perspective are provided. This review paves the way for rational design of 2D electrode materials for LIBs and Li–S battery applications and may provide a guide for future experiments.

1. Introduction

Energy storage has become an important issue of global concern because of the rapid growth of renewable energy applications and increasing demand on carbon emission reduction.[1,2] Among all the energy storage technologies, lithium-ion batteries (LIBs), because of their high energy density, have been widely used in portable electronic devices and electric vehicles.[3–5] Since the first appearance on the market by Sony company in 1991, LIBs have become the most widely used commercialized batteries so far. A typical LIB system may consist of Li intercalated transition metal oxide (cathode), graphite (anode), and complex of Li-ion with an organic compound as electrolyte (Fig. 1a). Current LIBs are still facing some technological challenges, such as capacity fading and low diffusion rates. With respect to these shortcomings, the exploration of new battery systems has never stopped, and one effective solution is to design and employ new electrodes.

As a promising alternative to LIB, the lithium-sulfur (Li–S) battery has gained attention since early 1960s.[6–8] It is constructed with metallic lithium anode and sulfur cathode immersed in electrolyte (Fig. 1b). On discharge, the Li metal anode is oxidized to Li^+, and Li^+ moves through electrolyte towards the cathode. At the cathode, Li^+ combined with sulfur to form various polysulfides (Li_2S_8, Li_2S_6, Li_2S_4, Li_2S_2 and Li_2S), and the ultimate product is Li_2S. Thus, the electrochemical reaction can be described as $2Li + S \leftrightarrow Li_2S$.[9,10] Li–S battery has many attractive features, including: (1) high theoretical specific capacity (1675 mA h g^{-1}) and high theoretical specific energy (2500 W h kg^{-1}), (2) natural abundance and low cost of sulfur.[11,12] However, Li–S batteries have not yet reached mass commercialization because of the low sulfur utilization and poor long-term cycling.[13,14] Thus, further investigation on suitable host materials for Li–S battery is in great demand.

Since the successful exfoliation of graphite into a single atomic layer of graphene, the study of two-dimensional (2D) materials has entered into a new era.[15,16] Thanks to the progress of high-performance computers and the development of accurate and efficient computational

* Corresponding author.
** Corresponding author.
E-mail addresses: yuen.tsang@polyu.edu.hk (Y.H. Tsang), aphhuang@polyu.edu.hk (H. Huang).

Production and Hosting by Elsevier on behalf of KeAi

https://doi.org/10.1016/j.matre.2023.100213
Received 19 January 2023; Received in revised form 3 March 2023; Accepted 14 March 2023
Available online 24 June 2023

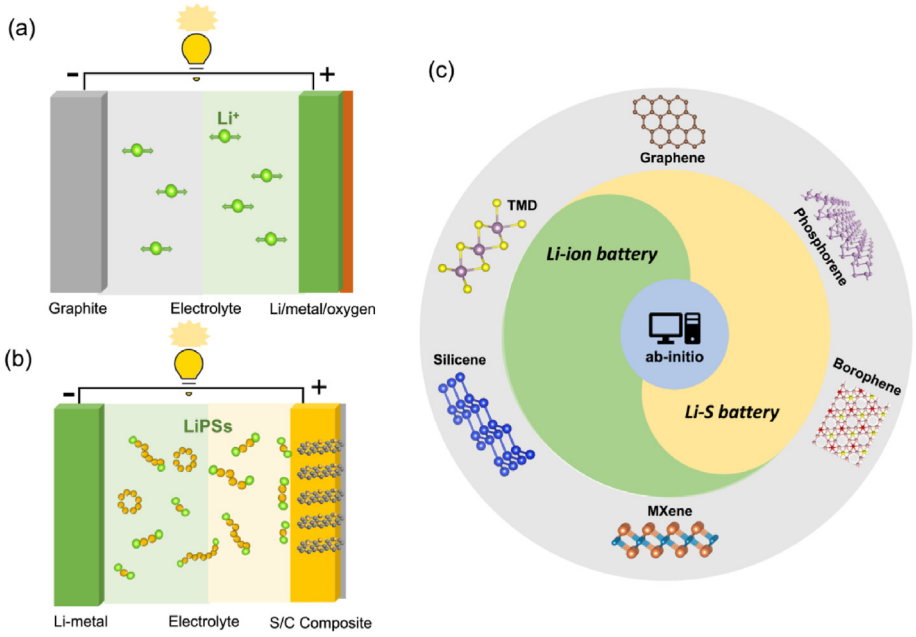

Fig. 1. (a) Schematic illustration of a typical Li-ion battery. (b) Schematic illustration of a typical Li–S battery. (c) Schematic illustration of 2D electrode materials in Li-ion and Li–S batteries based on *ab-initio* calculations.

methods, first-principles calculations have been widely used to explore the properties of known 2D materials and predict unknown 2D materials.[17] The great success of first-principles density functional theory (DFT) simulations lies in the fact that they can be independent of experiments, which provides fast and reliable estimations for some critical properties of the electrode materials, such as storage capacity, ion diffusion barrier, open-circuit voltage and so on. Thus, DFT simulations can greatly save experimental cost and research time.

Although there are some review articles about the 2D materials in metal-ion batteries,[18–24] a comprehensive review on theoretical design principles of promising 2D electrode materials and current progress in applications of 2D materials in Li-ion and Li–S batteries from a computational perspective is still lacking. In this review, our objective is to propose a general standard and summarize the current progress of potential 2D electrode materials in Li-ion and Li–S batteries based on DFT calculations (Fig. 1c). We hope this work could give a valuable insight into the design of next-generation rechargeable Li-ion and Li–S batteries.

2. Theoretical background

The general ideas of DFT of quantum systems were first proposed by Thomas and Fermi in 1927.[8,9] In the original Thomas-Fermi method, the kinetic energy of electrons is approximated as an explicit functional of the density, while the potential energy of electron density is equal to the local density at any given point. However, the Thomas-Fermi approximation is too crude, which lacks the essential physics and chemistry of a system. In 1964, Hohenberg and Kohn put forward two important theorems that allowed DFT to achieve unprecedented development.

Theorem I: The external potential (and hence the total energy) is a unique functional of the electron density.

$$E = E[n(\vec{r})] \tag{1}$$

Theorem II: The functional that delivers the ground-state energy of the system gives the lowest energy, if and only if the input density is the true ground-state density.

$$E[n(\vec{r})] > E_0[n_0(\vec{r})] \tag{2}$$

Thus, Hohenberg-Kohn theorem proved the existence of a general density functional which linked the energy of a system to its electron density distribution, but did not give a method of constructing this functional. This leads to the Kohn-Sham approach,[18,25] where the construction of an auxiliary system rests upon two assumptions: (1) The exact ground state density can be represented by the ground state density of an auxiliary system of non-interacting particles. (2) The auxiliary Hamiltonian is chosen to have the usual kinetic operator and an effective local potential $V_{\sigma\text{eff}}(r)$ acting on an electron of spin σ at point r.

The Kohn-Sham approach to the full interacting many-body problem is to rewrite the Hohenberg-Kohn expression for the ground state energy functional in the form:

$$E_{\mathrm{KS}} = T_{\mathrm{s}}[n] + \int \mathrm{d}r V_{\mathrm{ext}}(r) n(r) + F_{\mathrm{Hartree}}[n] + E_{\mathrm{II}} + E_{\mathrm{xc}}[n] \tag{3}$$

Here, $V_{\mathrm{ext}}(r)$ represents the external potential which is caused by the nuclei and any other external fields. E_{II} is the interaction between the nuclei. T_{s} is the independent-particle kinetic energy, which is given by:

$$T_{\mathrm{s}} = -\frac{1}{2}\sum_{\sigma}\sum_{i=1}^{N^{\sigma}} < \psi_{\mathrm{I}}^{\sigma} | \nabla^2 | \psi_{\mathrm{I}}^{\sigma} > = \frac{1}{2}\sum_{\sigma}\sum_{i=1}^{N^{\sigma}} \int d^3 r \left| < \nabla \psi_{\mathrm{I}}^{\sigma} > \right|^2 \tag{4}$$

and the classical Coulomb interaction energy of the electron density $n(r)$ interacting is defined as:

$$E_{\mathrm{Hartree}}[n] = \frac{1}{2}\int d^3 r d^3 r' \frac{n(r) n(r')}{|r - r'|} \tag{5}$$

Besides, all the many-body effects about exchange and correlation are grouped into the exchange-correlation energy E_{xc} that can be written as:

$$E_{\mathrm{xc}}[n] = < \hat{T} > - T_{\mathrm{s}}[n] + < \hat{V}_{\mathrm{int}} > - E_{\mathrm{Hartree}}[n] \tag{6}$$

Here, $[n]$ denotes a functional of the density n (r, σ) which depends upon both position in space r and spin σ. Through the Kohn-Sham approximation, a complex multi-electron problem can be transformed into a single-electron problem.

In general, with the development of DFT theory, almost all the materials can be explained and predicted well by DFT theory, and the computational efficiency has been greatly improved.

3. Principles of 2D materials design for batteries

2D materials have emerged as potential candidates for diverse applications such as superconductors, optoelectronic materials, and electrodes in batteries.[15,26] So far, nearly 50 compounds have been synthesized or exfoliated as single layers, which are far less than the experimentally known 3D compounds (~108,400).[27] In fact, recent high-throughput data studies indicate that hundreds of 2D materials could be exfoliated from known layered bulk crystals.[22,28–30] Thus, we believe those 2D monolayers that we already know are only the tips of a much larger iceberg and deserve further study.

First-principles calculations are commonly used in the prediction of new 2D materials and have achieved notable results.[31–35] For instance, Tománek et al. predicted the phosphorus carbide (α_1-PC) compounds through the unbiased structure searching technique, and this novel material was synthesized in the following year by Tan et al.[36,37] In this section, we systematically introduce the general criteria for designing novel 2D materials and the general conditions which judge whether a proposed 2D material is a promising electrode material, with all these standards established in the computational aspect. To be specific, the basic requirements for ideal host materials are shown in Fig. 2.[38] Above all, high stability (i.e., structural, dynamical, and thermal stability) is a prerequisite, since they work in the electrolyte and will be repeatedly cycled during the charge/discharge process. Secondly, materials with excellent electronic conductivity contribute to the electrochemical performance. Thirdly, high capacity is practically important to ensure a long service (or discharge) time for the battery. From the perspective of the rate capability of the battery, fast ion diffusion is also required. Moreover, for practical applications, accommodation of volume expansion, flexibility and lightweight of electrodes should be taken into consideration. Finally, low cost, large-scale synthesis, and environmental friendliness also need to be considered.

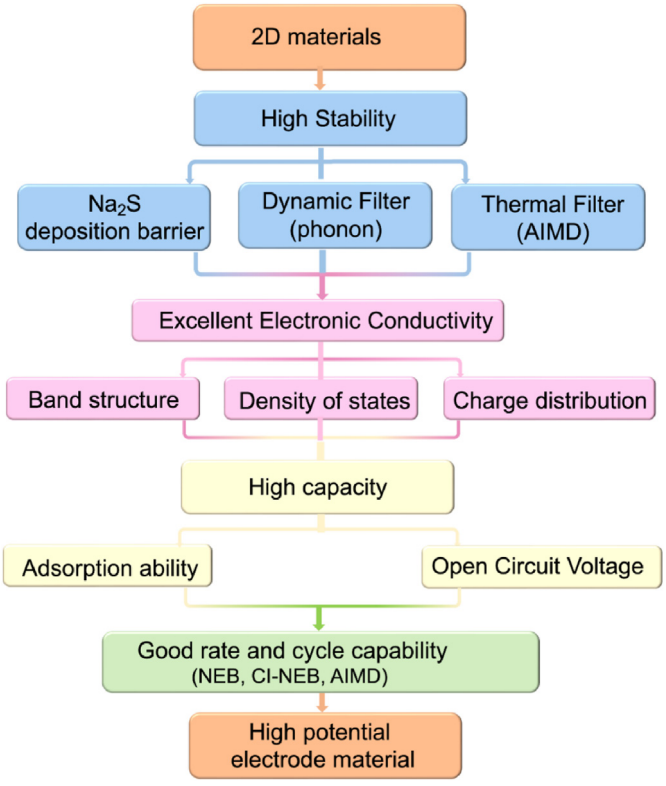

Fig. 2. Workflow for predicting the structural and physical properties of potential 2D electrode materials.

3.1. Stability

Electrode materials have high requirements for stability because they work in electrolytes and will be used repeatedly in the charge/discharge process. Therefore, the determination of 2D material stability is a prerequisite before studying its specific properties.[39]

3.1.1. Energy filter for the stability of 2D materials

Exfoliation energy: Exfoliation energy, which describes the energy required to peel off an atomic layer from the surface of a bulk material, is fundamentally important in the science and engineering of 2D materials.[32] A crucial criterion to judge the feasibility of mechanical exfoliation is energy cost, which is not only the key to explaining why existing 2D materials can be exfoliated experimentally, but also a guide to predicting whether an unknown 2D materials can be separated from their bulk counterparts. For instance, Mounet et al. proposed that the materials with an exfoliation energy less than 30 meV Å^{-2} can be easily exfoliated, and those with an exfoliation energy above 130 meV Å^{-2} are considered unable to exfoliate.[32]

Exfoliation energies are typically calculated by DFT methods, usually using the slab model. For the traditional slab model, exfoliation energy is defined as the energy difference before and after exfoliation of an atomic layer from the *N*-layer thick slab (Fig. 3a). Thus, the exfoliation energy E_{exf} can be described as:

$$E_{exf}(n) = (E_{II'} + E_{III'} - E_{I'}) / A \tag{7}$$

where $E_{I'}$, $E_{II'}$, and $E_{III'}$ are energies of the *N*-layer thick slab (I'), the exfoliated layer (II'), and the remaining (N−1)-layer slab (III'), respectively, and A refers to the in-plane area of the slab unit cell.

However, the slab method ignores possible lattice relaxation during the exfoliation process and requires a heavy computational load. Thus, great efforts have been made by many researchers.[40–45] For example, Shulenburger et al. proposed that the value of the exfoliation energy should lie in the range of interlayer binding energy of the bulk material and the binding energy of the two-atomic-layer system.[40] Recently, Jung et al. built up an impressive method to obtain the exfoliation energy of a given material which is exactly the ground-state energy difference between a single isolated layer and its bulk material (per atomic layer).[41] An and coworkers proposed a Green's function surface model, which can be used to study the exfoliation of ultrathin 2D layered materials from not only their bulk crystals but also semi-infinite substrates.[42] These newly developed methods greatly save computational resources and supplement the shortcomings of the traditional slab method.

Zhou et al. found that the alloying with Ti can significantly enhance the exfoliation of V_2AlC into V_2C MXene for LIB anodes.[46] This conclusion has been demonstrated by both experiments and first-principles calculations. Based on the XRD results, they found that with increasing amount of alloying Ti, the relative intensities of the residual $(V_{1-x}Ti_x)_2AlC$ phase decrease significantly, and the characteristic peaks of $(V_{0.7}Ti_{0.3})_2C$ are very strong, indicating that nearly pure 2D MXenes are obtained. Moreover, they also simulated the exfoliation process and estimated the exfoliation energy, as shown in Fig. 3b. It is obvious that alloying Ti significantly reduces the exfoliation energy for V_2AlC, which means the exfoliation of the bulk phases becomes much more energetically feasible.

Convex hull: To quantify the thermodynamic phase stability of materials, the construction technique of formation-energy convex hull (E_{hull}) has been developed.[49,50] In this technique, based on the systematical study of all possible mixtures of competing phases with the same compositions, a series of stable and meta-stable compounds are shown above or near the convex hull (Fig. 3c).[47] More specifically, compounds located at the energy convex hull, $E_{hull} = 0$, is a thermodynamically stable phase at 0 K. Those with $E_{hull} > 0$ but close to the convex hull can be considered thermodynamically meta-stable, and when $E_{hull} > 100$ meV/atom, the material is difficult to synthesize. So far, the thermodynamic phase

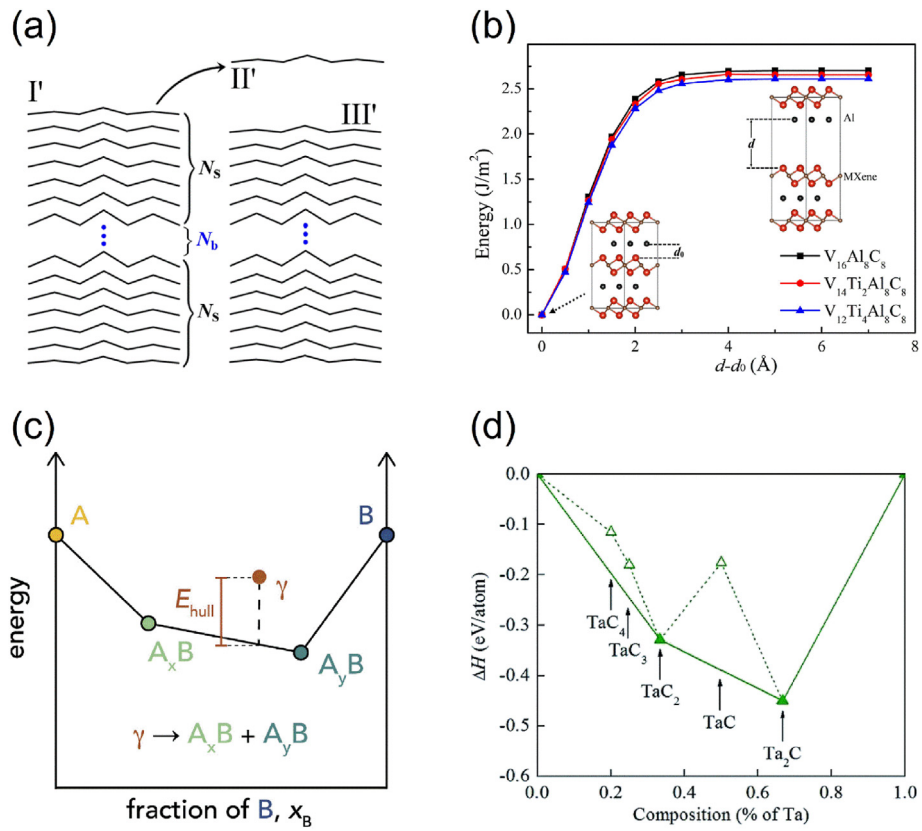

Fig. 3. (a) Schematic of traditional slab model to evaluate the exfoliation energies of 2D layered materials. Reproduced with permission from Ref. 42. (b) The calculated exfoliation energy vs separation d between MXene and Al layers. Reproduced with permission from Ref. 46. (c) Schematic of an energy convex hull. Reproduced with permission from Ref. 47. (d) Relative stabilities of 2D Ta_xC_y monolayers with respect to elemental Ta and graphene at 0 K. Reproduced with permission from Ref. 48.

stability of many new materials has been predicted by using E_{hull} metrics successfully.

Structure discovery algorithms are very important for the design and exploration of unknown stable crystal structures with fixed composition ratios. At present, various prediction codes have been developed, such as USPEX, AIRSS, and CALYPSO,[51–55] and aided by these codes, novel 2D materials with potential applications in batteries are proposed. As an example, Yu and coworkers performed first-principles structural searches to explore structural and phase stabilities of 2D Ta_xC_y ($x = 1$ and $y = 1$–4, or $x = 2$ and $y = 1$) in an effort to find promising anodes.[48] As shown in Fig. 3d, only TaC_2 and Ta_2C are lied on the convex hulls, which indicate that they are thermodynamically stable and feasible for experimental synthesis. However, the existence of 2D counterparts of a 3D parent compound does not ensure that the exfoliated monolayers would still be stable. Therefore, further research on the dynamic and mechanical stability of the material is still necessary.

3.1.2. *Dynamic filter for the stability of 2D materials*

An important criterion for dynamic stability is that the potential energy of the material should be a minimum against any combination of atomic displacements at equilibrium. The phonon filter is the most widely used approach in the analysis of the dynamic stability of 2D materials.[56–59] In this method, vibrational spectra are used to determine the stability of a certain material. Actually, the equilibrium condition can be described as a state in which all the phonons have real and positive frequencies in the harmonic approximation. Take the phonon dispersions of 2D-$MoSe_2$ and NbS_2 as an example.[60] For 2D-$MoSe_2$, all the frequencies in the phonon dispersion spectra are positive, which implies that the 2D material is dynamically stable (Fig. 4a and b). In contrast, for 2D-NbS_2, imaginary frequencies can be clearly observed (Fig. 4c and d), implying that it is unlikely to be realized experimentally and may lead to other structures through continuous lattice deformations and atomic displacements.

It is worth noting that the phonon analysis deals with small atomic displacements. Thus, it is hard to study complex lattices which involve lattice phase transformation or lattice reconstruction. Therefore, satisfying the phonon filter is a necessary but not sufficient condition to identify the dynamic stability of material.

3.1.3. *Thermal filter for the stability of 2D materials*

The stability of material under different temperature, at the first-principles level, is generally verified by *ab initio* molecular dynamics (AIMD) simulations.[62–64] One can observe the structural integrity of a certain material by performing the AIMD simulation at a fixed temperature within a specified time period. For example, Van Huis et al. used AIMD simulations to study a series of atomically thin transition metal oxides.[61] Their simulation results indicate that the hexagonal h-Mn_2O_3 phase is thermally stable due to the fact that the 300 and 700 K AIMD configurations reconstruct into the smoothly-tilted hexagons at 0 K (Fig. 4e and f). The square sq-MnO, on the other hand, has meta-stable character, which is thermally stable at 300 K (remained corrugated square structure) but unstable at 700 K (transformed into a hexagonal phase) (Fig. 4g and h). Finally, the h-TiO shows a thermally unstable character. After 300 K simulation, their AIMD final configurations relax into structures that are no longer atomically thin (Fig. 4i). Despite being a powerful tool, AIMD simulation requires a large computational resource.[65] Thus, they are limited to small systems with less than a few hundreds of atoms and very short physical timescale (tens to thousands of picoseconds).

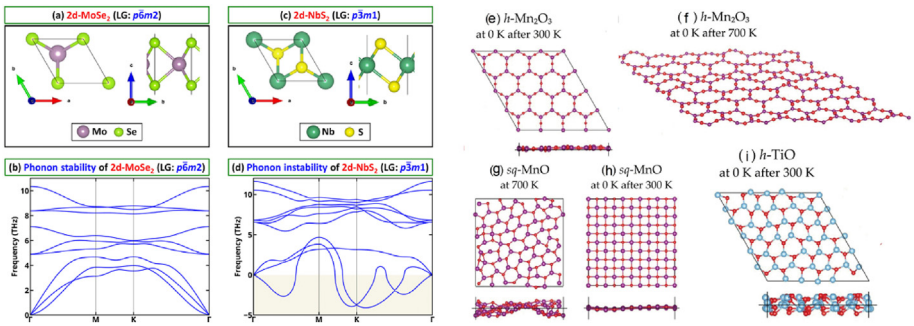

Fig. 4. Examples of application of phonon filter to analyze the stability of (a) 2D-$MoSe_2$ and (c) 2D-NbS_2, and corresponding phonon dispersions of (b) 2D-$MoSe_2$ and (d) 2D-NbS_2. Reproduced with permission from Ref. 60. AIMD simulation output configurations of (e) h-Mn_2O_3 at 0 K after 300 K, (f) h-Mn_2O_3 at 0 K after 700 K, (g) sq-MnO at 700 K, (h) sq-MnO at 0 K after 300 K, (i) h-TiO at 0 K after 300 K. Reproduced with permission from Ref. 61.

3.2. Electronic property

The electronic structure can be used to judge electrical conductivity, which is also a prerequisite for battery materials. There are several commonly investigated electronic properties for electrode materials to analyze their performance, including energy band structures, the density of states (DOSs), and charge density distribution.[39]

3.2.1. Band structure

The electronic band structure describes the range of energy levels that the electrons within a certain material may have, and it is directly related to the conductivity.[66] The band structure of a solid can be divided into three well-known parts: conduction band, valence band, and forbidden band. For an insulator, the band gap between the valence and conduction band is very large, and electrons transition from the valence to conduction bands almost cannot happen. In other words, insulators cannot conduct electricity. For a semiconductor, on the other hand, the band gap is small (usually from 0 to 3 eV). The valence band electrons can easily jump to the conduction band, forming conductive carriers. For a metallic band structure, an overlap between the conduction band and the valence band occurs, so the electrons can move to the conduction band without any obstacles, leading to good conductivity. It is worth noting that semiconductors can be divided into direct band gap and indirect band gap semiconductors according to the different paths of electron transition from the valence band to the conduction band.[67,68] Taking the bulk and monolayer MoS_2 materials as an example, the bulk MoS_2 is an indirect-gap semiconductor with a valence band maximum (VBM) at the Γ point and a conduction band minimum (CBM) along Γ–K symmetry lines (Fig. 5a),[69] while the monolayer MoS_2 is a direct-gap semiconductor with VBM and CBM located at the same K-point.

Li et al. used first-principles calculations to investigate the band structures of pristine and lithiated phosphorene (Fig. 5b).[70] According to their calculations, the pristine phosphorene shows semiconducting behavior, while after the Li-ion intercalation, the product shows a metallic character with zero band gap, indicating that the electronic conductivity of phosphorene can be enhanced by lithiation.

3.2.2. Density of states

The density of states (DOS) represents the number of states with a particular energy level that electrons are allowed to occupy, in other

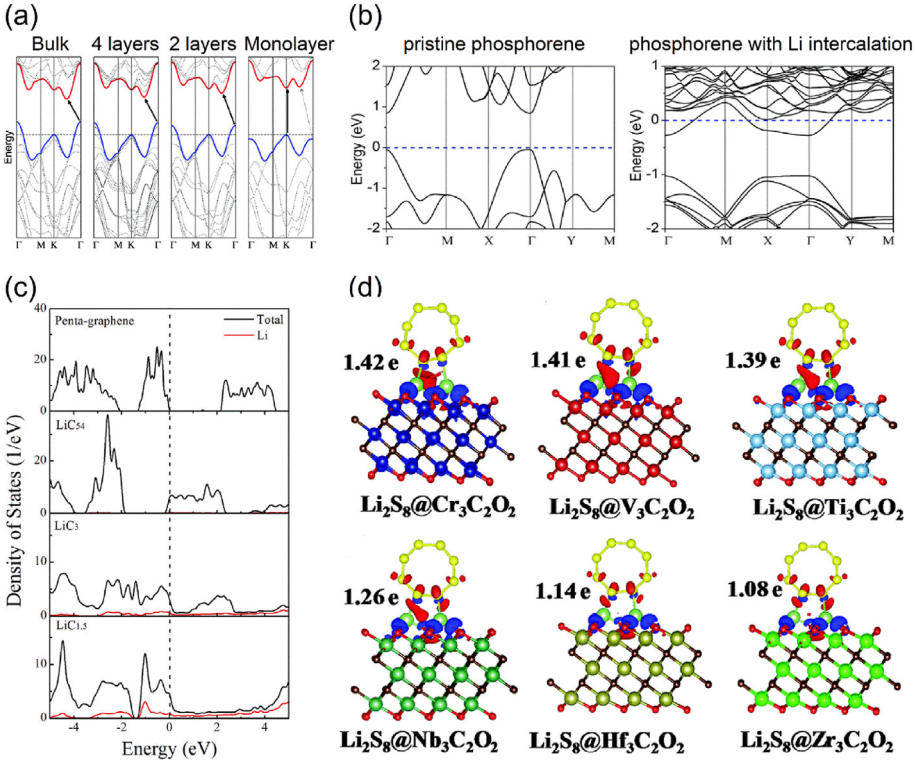

Fig. 5. (a) Evolution of the band structure of 2H–MoS_2 with decreasing thickness. Reproduced with permission from Ref. 69. (b) Electronic band structures of pristine phosphorene and phosphorene with Li intercalation. Reproduced with permission from Ref. 70. (c) DOSs of pure penta-graphene, LiC_{54}, LiC_3, and $LiC_{1.5}$. Reproduced with permission from Ref. 71. (d) Differential charge density between Li_2S_8 and $M_3C_2O_2$ surfaces ($Cr_3C_2O_2$, $V_3C_2O_2$, $Ti_3C_2O_2$, $Nb_3C_2O_2$, $Hf_3C_2O_2$ and $Zr_3C_2O_2$). Bader charge numbers indicate the number of electrons transferred from the LiPSs to the host material. Reproduced with permission from Ref. 72.

words, the number of electron states per unit energy per unit volume.[21] In principle, the DOS can be understood as a more intuitive visualization of the band structure. From DOS, one can also analyze the energy gap characteristics. If the DOS value at the Fermi level is zero, the system can be a semiconductor or an insulator. Otherwise, the system is metallic. The partial density of states (PDOS) related to certain atoms or orbitals can give more detailed bonding information.

From a recent example of DOS analysis, Xiao and coworkers found that the doping of Li^+ in penta-graphene can affect its electronic structure and improve its electrochemical performance in LIBs.[71] The pure penta-graphene exhibits semiconductor properties with a calculated band gap of 2.33 eV. After adopting one Li atom on the penta-graphene (LiC_{54}), this new system showed a metallic character (Fig. 5c). With increasing content of Li atoms (LiC_3 and $LiC_{1.5}$), the electronic conductivity of penta-graphene is further enhanced. This semiconductor-to-metal transition greatly facilitates the charging and discharging rate in LIBs.

3.2.3. Charge density distribution

The charge density distribution figures can theoretically show the chemical environment of the atoms in a certain material, which fills the gap that the charge distribution is difficult to be directly measured in experiments. In DFT calculation, the effect of adatom adsorption on charge distribution is calculated by the differential charge density, which is defined as the difference between the valence charge densities before and after bonding[73,74]:

$$\Delta\rho = \rho_{\text{sub+adsorp}} - \rho_{\text{sub}} - \rho_{\text{adsorp}} \tag{8}$$

where $\rho_{\text{sub+adsorp}}$, ρ_{sub} and ρ_{adsorp} represent the charge density distribution of the substrate-adatom system, bare substrate, and adsorption atom, respectively. For instance, Li et al. investigated the electronic structures of Li_2S_8 adsorped on $M_3C_2O_2$ surfaces (M = Cr, V, Ti, Nb, Hf, and Zr) (Fig. 5d) through charge density distribution.[72] For all six $M_3C_2O_2$ systems, the electron transfer from Li_2S_8 to substrates can be observed, indicating the strong interactions. This can be further ascribed to the strong covalent bonds between Li and O. Moreover, the amount of charge transfer in a certain material can be estimated quantitatively by methods such as the Bader charge analysis.[75]

3.3. Capacity

In practical applications, the storage capacity is a key indicator of electrode performance and a target for improvement.[39]

3.3.1. Adsorption

The adsorption of ions plays a key role in the electrochemical reaction of battery materials. Therefore, the adsorption kinetics must be considered when designing new electrodes, since it has a great impact on the capacity of the cells.[76–78] Indeed, the adsorption energy between electrodes and metal atoms should be moderate.[79,80] Too weak adsorption results in a low capacity of the battery. However, too strong binding may lead to difficult desorption of the adatoms or the decomposition of adsorbed species, thereby deteriorating the cycle performance of the material.

The adsorption energy between substrate and adatoms can be calculated as follows[81,82]:

$$E_{\text{ad}} = E_{\text{sub+adsorp}} - E_{\text{sub}} - E_{\text{adsorp}} \tag{9}$$

where $E_{\text{sub + adsorp}}$ is the total energy of substrate-adatom system, E_{sub} and E_{adsorp} are the total energy of the pristine system and the total energy of adsorbed atoms, respectively. Theoretically, smaller adsorption energy can bring about more favorable interaction between the substrate and the adatoms. Through comparing the E_{ad} values at different sites, the preferred adsorption sites can be determined.

For instance, to investigate the nature of metal atom adsorption on MoN_2 monolayer, Yang's group discussed four possible adsorption sites (denoted as S_1–S_4) as depicted in Fig. 6a.[83] They found that all the studied metal atoms can be adsorbed on MoN_2 monolayer and the adsorption above the center of the honeycomb lattice (S_3 site) is the most favorable adsorption site.

3.3.2. Open circuit voltage

Open circuit voltage (OCV) is a crucial indicator to determine the capacity and also the energy density of battery materials.[85,86] A positive value of voltage indicates that the adsorbed atoms can successfully adsorbed on the substrate surface, while a negative value means that the adsorbed atoms are more inclined to form clusters rather than be adsorbed on the substrate surface. Thus, when the OCV value drops to 0 eV, the material is considered to have reached its maximum capacity.

The average OCV within the adatoms coverage range from x_1 to x_2 can be estimated by:

$$OCV \approx \frac{\Delta G}{(x_2 - x_1)} \tag{10}$$

where ΔG is approximately equal to the change in internal energy ($\Delta G = \Delta E + p\Delta V - T\Delta S$), because volume effects and entropy make little contribution to the voltage at room temperature (<0.01 V).

For example, the average cell voltage of $LiCoO_2$ lithiation range ($x_1 \le x \le x_2$) can be estimated as:

$$V_{\text{ave}} = -\frac{E_{\text{Li}_{x2}\text{CoO}_2} - E_{\text{Li}_{x1}\text{CoO}_2} - (x_2 - x_1)E_{\text{Li}_{(s)}}}{(x_2 - x_1)e} \tag{11}$$

The relationship between the formation energy and voltage profile has been perfectly illustrated by Ceder's group.[87] And the computational voltage profile has been proved to fit well with the experimental one for sodium intercalation in Na_xMnO_2 system.

Based on the OCV, the maximum adatom content x_{max} can be evaluated, and the maximum capacity C_{M} (mA h g^{-1}) can be further calculated as:

$$C_M = \frac{1}{M_{\text{sub}}}\left[x_{\text{max}} \times z \times F \times 10^3\right] \tag{12}$$

where z is the valence number, F is the Faraday constant (26.810 Ah mol^{-1}), and M_{sub} is the atomic mass of substrate material.[88]

Shenoy's group evaluated the OCVs as a function of the concentration of adatoms (Li, Na, K, and Ca) by varying x in the $Ti_3C_2M_x$ system.[89] According to Fig. 6b, the OCV of Na, K, and Ca decrease as x increases, while Li is less sensitive to the variance of x in the range $x \le 1$ and starts to decrease when $x > 1$. According to their calculations, the OCVs for Li, Na, K, and Ca are 0.413, 0.137, 0.128, and 0.087 V, respectively. Therefore, the corresponding theoretical capacities of $Ti_3C_2Li_x$, $Ti_3C_2Na_x$, $Ti_3C_2K_x$ and $Ti_3C_2Ca_x$ systems are calculated to be 447.8, 351.8, 191.8, and 319.8 mA h g^{-1}, respectively (Fig. 6c).

3.4. Ion diffusion mechanism

The ion diffusion process is closely related to the rate performance of a cell and has instructive significance for studying the electrochemical performance of electrode materials.[39] The current mainstream research methods are the nudged elastic band (NEB) method, modified climbing-image nudged elastic band (CI-NEB) method, AIMD method and Monte Carlo simulation.

3.4.1. NEB method

NEB method is efficient for studying the ion diffusion.[90] The aim of this approximation is to find the minimum energy path (MEP) of a mobile ion and to obtain the corresponding energy barrier. Along the MEP, the maximum energy position on the potential energy surface is the saddle

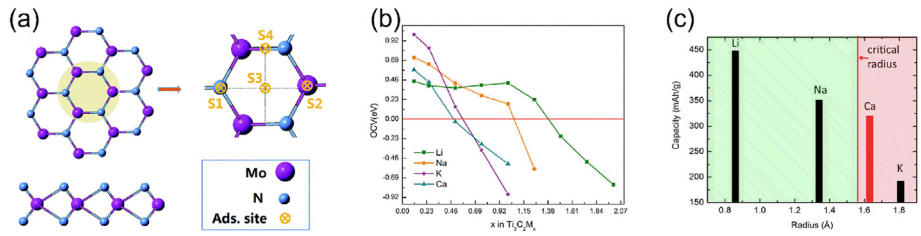

Fig. 6. (a) Atomic structures and possible adsorption sites of MoN_2 monolayer. Reproduced with permission from Ref. 83. (b) OCV changes with adatom content for the single-side adsorption of Li, Na, K, and Ca on Ti_3C_2 surface. (c) Relationship between capacity and ionic radius for adsorption on both sides of Ti_3C_2 surface. Reproduced with permission from Ref. 84.

point, and the energy of the highest saddle point is usually considered as the energy barrier for ion diffusion on the material.

In the calculation process, a set of image replicas (R_0, R_1, R_2, …, R_N) of the system have been constructed between the initial (R_0) and final state (R_N), and the number of images is usually chosen based on the length of the diffusion path (Fig. 7a).[17] For NEB method, the basic feature is the force projection, which decomposes the true force ($\nabla E(\vec{R}_i)$) and the spring force ($\vec{F}_i^s$) into components parallel ($|_{\|}$) and perpendicular ($|_{\perp}$) to the path by "nudging". Thus, it can ensure that the spring force will not interfere with the convergence of the elastic band to the MEP and that the true force will not affect the distribution of images along with the MEP. The total force acting on an image ($\vec{F}_i$) can be described by the following equation:

$$\vec{F}_i = \vec{F}_i^s|_{\|} - \nabla E\left(\vec{R}_i\right)|_{\perp} \tag{13}$$

An example of a NEB calculation of the Li-ion diffusion path and energy barrier in two-dimensional phosphorene is shown in Fig. 7b and c.[91] The authors discussed two possible diffusion paths: one is in-plane diffusion, and the other is out-of-plane diffusion. Based on their results, the diffusion of Li is preferred in the in-plane direction of the phosphorene monolayer with a barrier of 0.76 eV.

It should be noted that the key point of NEB method is to ensure that the highest saddle point is found. In fact, it is common for MEPs to have one or more intermediate minima, but there is no clear range about where the highest saddle point should be. If the path is curved at the saddle point, it may lead to an overestimation or underestimate of the saddle point energy. To solve this problem, one could run a second elastic band between the two images adjacent to the barrier to get a more accurate estimation of the saddle point energy, but this would require much more computational effort.

3.4.2. *Climbing-image NEB method*

The CI-NEB method as a modification of the NEB one, is more accurate for saddle point search.[93] As shown in Fig. 7a, using the CI-NEB method to find the MEP can not only retain the similar shape as obtained in the NEB calculation, but also keep the climbing image with a rigorous converge on the highest saddle point. By using the same number of images in CI-NEB, a more accurate activation energy than the regular NEB would be obtained, while this does not add any significant calculation workload.

The force on CI-NEB method is not given by Equation (13) but rather by:

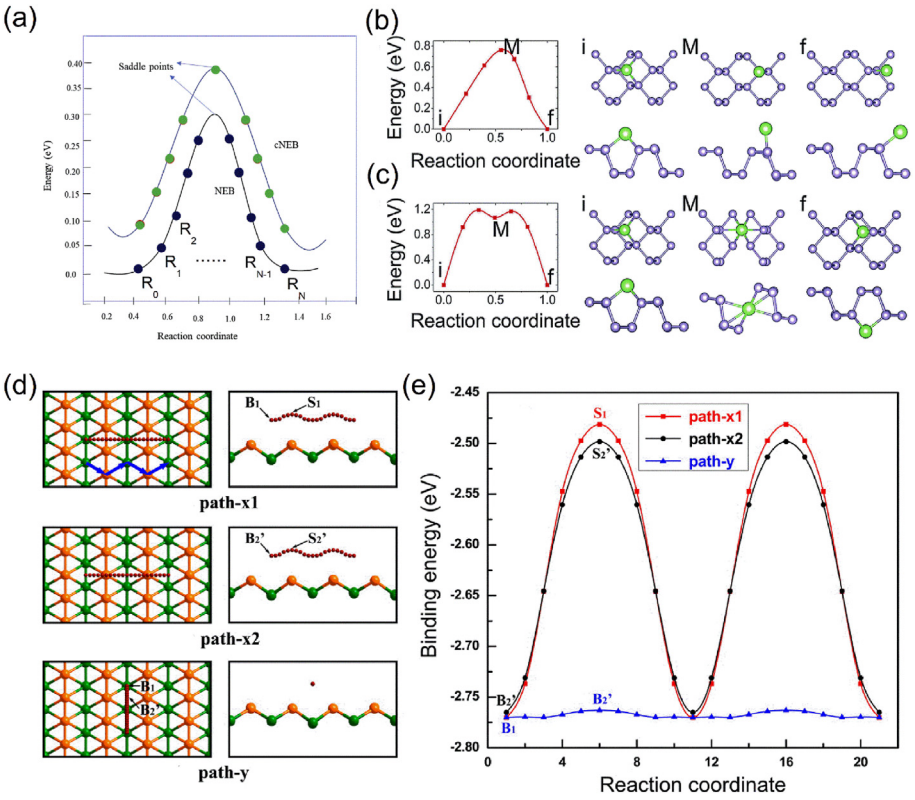

Fig. 7. (a) Saddle points obtained from NEB and CI-NEB modifications. Reproduced with permission from Ref. 17. Energy barrier and diffusion path of a Li atom on the phosphorene monolayer: (b) in-plane diffusion and (c) out-of-plane diffusion. Reproduced with permission from Ref. 91. (d) Top (left panel) and side (right panel) views of Li diffusion on borophene surface along path-x1, path-x2, and path-y. Corresponding binding energies along the diffusion pathways are shown in Fig. 7e. Reproduced with permission from Ref. 92.

$$\vec{F}_{i_{max}} = -\nabla E\left(\vec{R}_{i_{max}}\right) + 2\nabla E\left(\vec{R}_{i_{max}}\right)|_{\|} \quad (14)$$

This is the full force due to the potential with the component along the elastic band inverted. Here, i_{max} represents the highest saddle point, and $\vec{F}_{i_{max}}$ is the total force acting on a maximum energy image. $\nabla E(\vec{R}_{i_{max}})$ and $\nabla E(\vec{R}_{i_{max}})|_{\|}$ are true forces at the highest saddle point and the parallel ($|_{\|}$) component. The maximum energy image is not affected by the spring forces at all.

According to transition state theory, the ion diffusion rate can be expressed as[94,95]:

$$k(T) = \nu^* \exp\left(-\frac{\Delta E^+}{k_B T}\right) \quad (15)$$

where T is the temperature, and k_B is the Boltzmann constant. The activation energy ΔE^+ represents the energy difference between the transition state and the initial one.

The vibrational prefactor $\nu^\star$ can be expressed as:

$$\nu^\star = \frac{\prod_i^{3M} \nu_i}{\prod_j^{3M-1} \nu_j'} \quad (16)$$

where M is the total number of atoms, and ν_i is the corresponding normal mode frequency.

Zhang and coworkers predicted that the borophene layer has ultrahigh diffusivity along an uncorrugated direction.[92] As depicted in Fig. 7d, they considered three diffusion pathways, i.e., path-x1, path-x2, and path-y. For path-x1 and path-x2, the energy barriers are calculated to be 0.289 and 0.267 eV, respectively. The diffusion pathway of path-y shows a rather small energy barrier of 0.007 eV, indicating that the Li-ion diffusion along the uncorrugated direction is much easier than that along the corrugated direction (Fig. 7e). Such an anisotropic diffusion behavior can be attributed to the anisotropic structure of the borophene layer.

To conclude, computational studies based on the NEB and CI-NEB methods have significantly increased the understanding of the static energy state of ion migration pathways in electrode materials. However, one of the difficulties in NEB calculations is the initial guessing of ion-hopping sites and pathways, which becomes much more complicated when it comes to some highly disordered and low symmetry lattice systems.

3.4.3. AIMD method

The real-time ion dynamics from AIMD simulations could show the diffusion mechanisms directly without the need for a priori assumption of diffusion pathways.

The diffusivity D from AIMD simulations can be calculated from the Einstein–Smoluchowski equation:

$$D = \frac{1}{2d\Delta t}\frac{1}{N}\sum_{i=1}^{N} < \left|\vec{r}_i(t+\Delta t) - \vec{r}_i(t)\right|^2 > \quad (17)$$

where $\left|\vec{r}_i(t+\Delta t) - \vec{r}_i(t)\right|^2$ represents the mean-squared displacement (MSD) of the ions, $r_i(t)$ corresponds to the position of the ion i at time t in the AIMD calculation, N is the total number of ions, and d is the lattice size.

The diffusivity D at different temperatures can be fitted from the Arrhenius relationship[65,96,97]:

$$D = D_0 \exp\left(-\frac{E_a}{k_B T}\right) \quad (18)$$

Through this fitting, the overall activation energy E_a and the pre-exponential factor D_0 are obtained. Then, the diffusivity can be evaluated at different temperatures.

The ionic conductivity σ can be further evaluated by Nernst-Einstein equation:

$$\sigma(T) = \frac{N_{Li} q^2}{V k_B T} D(T) \quad (19)$$

where V is the volume of the simulation model, and q is the charge.

A typical example is the study conducted by Mo et al. who determined the diffusion pathways and the corresponding diffusion coefficients of $Li_{10}GeP_2S_{12}$ (LGPS) by AIMD simulations.[98] Three facile Li diffusion pathways were observed, and one of them is a one-dimensional diffusion channel along the *c*-direction, which is consistent with the hypothesis of Kamaya et al.[99] Two additional diffusion pathways in the *ab* plane were first proposed and were confirmed five years later in neutron powder diffraction experiments by Weber et al.[100] Besides, the overall activation barrier (0.21 eV) and Li^+ conductivity (9 mS cm^{-1}) were also calculated, which are in remarkable agreement with experimental results, thus confirming the accuracy of AIMD simulations for the study of diffusion mechanisms in crystal structures. It is worth noting that a large number of ion migration events are absolutely necessary during the AIMD simulation in order to obtain convincing diffusion properties.

3.4.4. Monte Carlo simulation and cluster expansion method

Monte Carlo (MC) simulation can well overcome the limitations of computing power for first principles and extend the system size to millions of atoms.[101] However, discussing the diffusion mechanism involves large-scale atomic emulations that need the cluster expansion method as an effective medium.[102–104]

The cluster expansion method is a powerful tool for linking quantum mechanics with large-scale atomic emulations, which usually works as a bridge between first-principles calculations and MC simulations.[105,106] The method is mainly divided into the following two steps. Firstly, the ground state energies of a small number of configurations are calculated by first principles. By fitting the output data obtained from the first-principles, an important effective cluster interaction (ECI) can be achieved. Secondly, the cluster expansion can be used as a Hamiltonian for MC simulations to calculate the energy of larger supercells. Finally, material properties (such as phase diagram, structure and ion diffusion mechanism) can be obtained from the simulation output.

For example, Van der Ven et al. used the above mentioned method to study lithium ion hopping mechanism and diffusion barrier in Li_xCoO_2 system.[107] First they used the first principles to identify the possible lithium migration mechanisms and found two lithium ion migration paths (ODH and TSH) which greatly depend on the lithium-vacancy arrangement environment. Then, they used cluster expansion method to calculate the activation barrier in every local lithium vacancy environment. Finally, they implemented this procedure of calculating activation barriers in kinetic Monte Carlo simulations to calculate lithium diffusion coefficients. The average activation barrier decreased with the increase of Li concentration.

4. Two-dimensional electrode materials for LIBs

4.1. 2D carbon-based materials

Carbon-based materials are widely used as electrode materials for Li-ion batteries due to their high stability and excellent conductivity. Among them, graphene is a typical 2D representative. Up to now, a large number of 2D carbon materials have been found, and some of them have been proved to have great potential as lithium-ion electrode materials.

4.1.1. Graphene

The single atomic layers of graphene were successfully exfoliated from graphite by Novoselov and coworkers in 2004.[108] Owing to its irreplaceable unique features, graphene has been intensively studied as

Li-ion battery anodes in recent years.

DFT calculations revealed that a single Li atom cannot be adsorbed on the defect-free single-layer graphene (SLG) surface. On the contrary, Li atoms prefer to form clusters on the surface of graphene. For example, Lee et al. discussed Li adsorption and intercalation in single-layer and few-layer graphene.[109] They found that no Li atoms could be arranged on the surface of SLG due to the positive absorption energy (Fig. 8a). Moreover, they found Li atoms could intercalate into few-layer graphene, while the capacity is far below that of bulk graphite. This is highly in agreement with the in-situ Raman spectroscopy results obtained by Pollak et al. who found low surface coverage of Li (about 5%) on SLG and few-layer graphene, equivalent to the capacity of LiC_{20}.[110] Fan et al. proposed that, under some favorable conditions, the formation of small Li clusters on the surface of defect-free graphene is possible (Fig. 8b).[111] However, it should be noted that with increasing Li content, Li dendrites can be formed and thus poses stability issues. The process of Li cluster formation on graphene has been studied by Liu and coworkers.[112] They believed that the driving force for the nucleation could be the low-energy electrons localized inside the Li clusters.

Regarding the poor Li adsorption on pristine graphene and the Li clustering, recent achievements have proved that heteroatom-doped graphene could enhance the storage capacities. For example, Wu et al. found that the layered nitrogenated holey graphene (C_2N) nanosheets can achieve an extremely high specific capacity of Li storage up to 2939 mA h g^{-1}, which is nearly 6–8 times that of graphite (Table 1).[121] Si-doped graphene can not only improve the storage capacity (1171 mA h g^{-1}) of Li atoms but also reduce the volume expansion effect (0.4%).[122] Germagraphene can achieve a high Li storage capacity up to 1734 mA h g^{-1} at the optimal Ge concentration, $C_{17}Ge$.[123] Compared with monodoping, the integration of two heterogeneous species into graphene is easier to achieve. Denis's group studied the adsorption of Li onto X-monodoped (X = Al, Si, P, and S) and XY dual-doped graphene (Y=B, N, and O).[124] Based on the analysis of the 18 different systems, the researchers found that the performance of dual-doped graphene is better than the mono-doped one due to better control of the interaction energy of Li onto graphene and the electronic properties of graphene.

It has been found that the presence of defects can improve the ratio of Li/C greatly, and different types of defects significantly affect the performance of electrodes.[125] Generally, the common defects can be classified as: single vacancy (SV), divacancy (DV), Stone-Wales (SW) defect and grain boundary (GB). Okamoto discussed the Li insertion and adsorption in three types of graphene (defect-free, defective, and hydrogen-terminated carbon vacancies),[126] and found that the carbon vacancies strongly enhance the interaction between Li and graphene because of the dangling bonds. Datta et al. further discussed the Li adsorption on graphene with different percentages of DV and SW defect densities.[113] They found that the underlying charge-transfer mechanism is responsible for enhanced adsorption on defective graphene (Fig. 8c). Moreover, for the maximum possible DV defect density, Li storage capacities have been predicted to be 1675 mA h g^{-1}, while for SW defects, the maximum capacity can be up to 1100 mA h g^{-1}. Moreover, the heteroatom-doped defective graphene also exhibits great potential as electrode. Hardikar and coworkers discussed five different types of boron-doped defective graphene, including: (i) DV, (ii) SW, (iii) pristine boron doped, (iv) boron doped mono-vacancy, (v) one-, and two-boron doped DV.[127] Among these systems, two-boron doped mono-vacancy graphene has been predicted as the most suitable anode material because of the low energy barrier of 0.31 eV and good adsorption effect. Moreover, the GBs of graphene which consist of pentagons, heptagons and octagons also exhibit great influence on the performance of Li adsorption and diffusion on graphene.[128]

4.1.2. *Graphene-like 2D carbon structures*

Apart from graphene, various 2D carbon allotropes have been predicted theoretically, some of which have also been prepared experimentally.

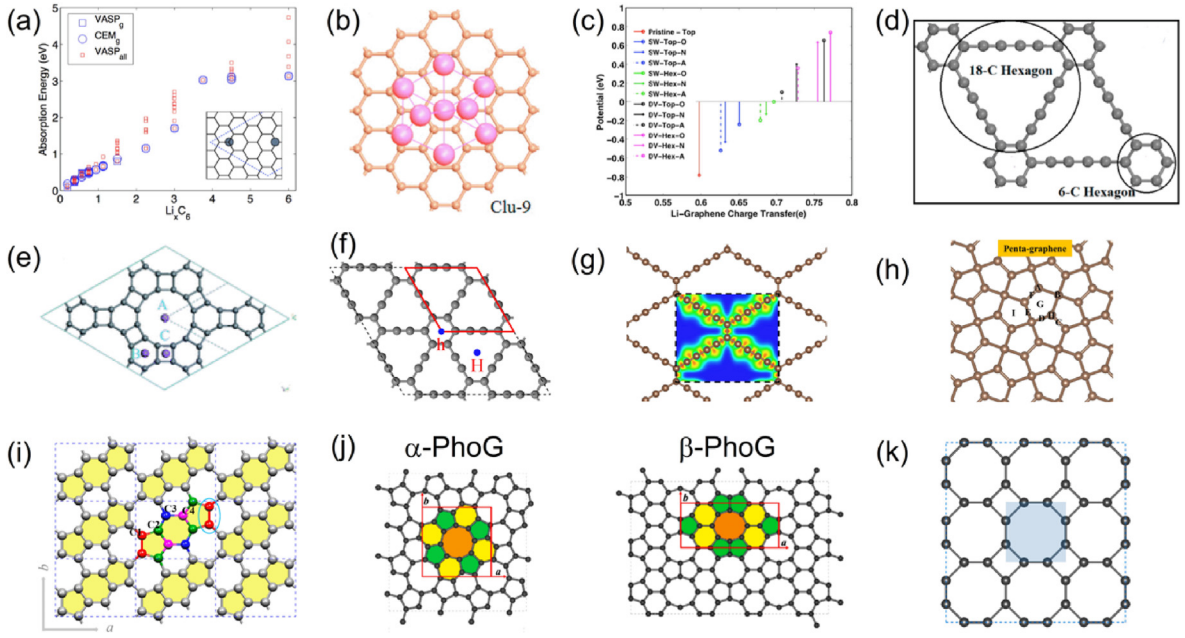

Fig. 8. (a) Absorption energy on defect-free single-layer graphene predicted by the DFT calculations. Reproduced with permission from Ref. 109. (b) Schematic representations of the Li_9 adsorbed on graphene. Reproduced with permission from Ref. 111. (c) Charge-transfer vs lithiation potential on defective graphene. Reproduced with permission from Ref. 113. (d) Optimized geometries of graphdiyne. Reproduced with permission from Ref. 114. (e) Layer structure of graphenylene in a 2 × 2 supercell. Reproduced with permission from Ref. 115. (f) 2 × 2 supercell of monolayer graphyne. Reproduced with permission from Ref. 116. (g) The structure of carbon ene-yne. Reproduced with permission from Ref. 117. (h) Schematic illustration of all the possible Li adsorption sites on penta-graphene. Reproduced with permission from Ref. 71. (i) Optimized structure of ψ-graphene with the *s*-indacene skeletons highlighted in yellow. Reproduced with permission from Ref. 118. (j) Structures of phographene. Reproduced with permission from Ref. 119. (k) Crystal structures of T-graphene. Reproduced with permission from Ref. 120.

Table 1
Summary of performance parameters for 2D materials used in Li-ion batteries.

Electrode materials	Adsorption energy (eV)	Diffusion barrier (eV)	Capacity (mA h g^{-1})	Ref.
Pristine G	−1.463	0.311	N.A.	109
N-doped G	−2.868	0.356	2939	121
Si-doped G	−1.54	0.1333	1171	122
Ge-doped G	−0.94	0.151	1734	123
GDY	−2.63	0.18	N.A.	114
CEY	−1.098	0.58	2680	117
Penta-G	−0.30	0.17	1489	71
ψ-graphene	−0.64	0.265	372	118
α-PhoG	−0.38	0.28	892	119
β-PhoG	−0.38	0.15	557	119
T-graphene	−1.155	0.44	2233.2	120
Borophene	−1.12	0.0026	1860	131
β_{12} borophene	−1.766	0.66	1984	132
χ_3 borophene	−1.433	0.6	1240	132
β_1^s	−1.62	0.40	1239.56	133
BG	−1.92	0.33	1653	134
h-borophene	−1.06	0.53	5268	135
Borophane	−2.58	0.27	504	136
Phosphorene	−1.8	0.76	432.79	91
Blue phosphorus	−2.02	0.12	865	137
Silicene	−2.27	1.33	1196	138
MoSSe	−2.8	0.23	776.5	139
VS_2	−2.13	0.22	466	140
ReS_2	−2.28	0.33	428	141
$WS_2/NbSe_2$	−3.26	0.18	842.4	142
Ti_3C_2	−3.535	0.07	320	143
$Ti_3C_2S_2$	−1.94	0.25	462.6	144
Ti_2N	−0.71	0.017	487	145
Ti_3CN	−2.57	0.024	320	146
V_3C_2	−1.01	0.04	606.42	74
V_2C	−1.573	0.045	940	147
Mo_2C	−0.97	0.043	526	148
Mn_2C	−1.93	0.05	879	149
Sc_2C	−0.31	0.018	462	150
Nb_2C	−0.71	0.036	305	151
Hf_3C_2	−2.23	0.027	1034.70	152
TiNbC	−0.802	0.018	351	153
VC_2-α	−0.61	0.51	1073	154
VC_2-β	−0.65	0.11	1073	154
MoN_2	−1.81	0.78	432	83
NiC_3	−0.89	0.5	1698	155

As a carbon allotrope, graphdiyne (GDY) consists of a *sp*- and sp^2-hybridized carbon network (Fig. 8d).[114] For GDY monolayers, it shows high storage capacity comparable to LiC_3, and excellent mobility with diffusion barriers from 0.17 to 0.84 eV. Graphenylene, because of its unique dodecagonal holes, exhibits a low energy barrier (<0.99 eV) both on and through graphenylene layers (Fig. 8e).[115] Monolayer and bilayer graphenylene compounds with the maximum Li contents are Li_3C_6 and $Li_{2.5}C_6$, which correspond to capacities of 1116 and 930 mA h g^{-1}, respectively. Zhang et al. found the capacity of graphyne increases with strain (Fig. 8f).[116] Under the 12% strain, the Li capacity of the Li_6C_6 configuration for graphyne reaches 2233 mA h g^{-1}. Moreover, the structure of graphyne monolayer can keep intact below the 16% strain. Carbon ene-yne (CEY), another graphyne-based structure, was successfully synthesized by the solvent-phase reaction recently (Fig. 8g).[117] CEY exhibits a high theoretical charge capacity of 2680 mA h g^{-1} for Li-ion batteries (Table 1). Penta-graphene was first proposed by Zhang et al. who found that a single Li-ion prefers to absorb on the A-site of penta-graphene with the adsorption energy of −0.30/−0.41 eV (Fig. 8h).[71] ψ-graphene, which can be synthesized by using *s*-indacene derivatives as molecule precursors, has the lowest energy among all hitherto reported 2D allotropes of carbon composed of 5–6−7 carbon rings (Fig. 8i).[118] Thomas et al. predicted that ψ-graphene possesses a capacity of 339 mA h g^{-1} and a diffusion barrier less than 0.21 eV[129] α- and β-phographenes (PhoG) consist of 5-, 6- and 8- membered rings that show great potential as electrodes (Fig. 8j).[119] Both systems exhibit fast Li mobility and low average OCV. Particularly, α-PhoG shows a higher theoretical specific capacity of 892 mA h g^{-1} ($Li_{2.4}C_6$). Because of low atomic mass and special periodic lattice structure, T-graphene shows an extremely high capacity of 2233.2 mA h g^{-1} (Fig. 8k).[120] Moreover, it exhibits good cycling performance with very small lattice change of about 1.0% after lithium adsorption.[130]

4.2. Elemental 2D materials

4.2.1. Borophene

Boron is the fifth element in the periodic table and located just near carbon. In 2015, 2D borophene (δ_6B) was successfully synthesized by Mannix et al. Before that, a large variety of planar 2D boron sheet structures have already been theoretically predicted.[156–160] Very recently, triangular borophene (ΔB), β_{12}-borophene (β_{12}B), and χ_3-borophene (χ_3B) have been successfully grown on some metal (Ag (111), Cu (111) and Au (111)) surfaces with novel physicochemical properties.[161–163] Because of the metallicity, light weight and the porous configurations, 2D borophenes have been expected as promising electrode materials.

Jiang et al. suggested that borophene can be applied to Li-ion battery with ultrahigh theoretical capacity.[131] They found that the most stable site for Li adsorption is above the top of boron atoms (T_F site) with the adsorption energy of −1.12 eV (Fig. 9a), and the binding energy between Li atoms and borophene generally decreases with the increase of the Li content. In addition, the capacity of borophene is predicted to be 1860 mA h g^{-1}, which is four times higher than that of graphite (372 mA h g^{-1}). Besides, borophene as an anode in Li-ion battery also exhibits ultrahigh rate capability.[92] Because of the anisotropic ripple structure, the energy barrier of the Li-ion along uncorrugated direction is predicted to be 0.033 eV, which is highly energetically favorable compared with the corrugated direction (0.274 eV) (Fig. 9b). This finding suggests that lithium diffusion on borophene can be extremely fast.

Different types of borophene exhibit different properties as electrodes. For β_{12} borophene and χ_3 borophene, the full lithium storage phases correspond to Li_8B_{10} and Li_8B_{16} with theoretical specific capacities of 1984 mA h g^{-1} and 1240 mA h g^{-1}, respectively.[132] Borophene β_1^s is a semiconductor with a band gap of 0.74 eV.[133] Theoretical calculations find that it shows metallic characteristics after lithiation, thus improving the conductivity of the electrode materials. A new structure B_G has been found to show special electronic property with double Dirac cones.[134] The energy barriers of Li-ion and Li vacancy diffusion on B_G are calculated to be 330 and 110 meV, respectively, which imply fast charge and discharge ability for B_G as an anode material. It is worth noting that the honeycomb borophene (h-borophene) exhibited the highest theoretical capacity (5268 mA h g^{-1}) among all the 2D materials for the LIBs (Fig. 9c).[135] This can be explained by the non-buckled structure of h-borophene which has the least molar mass per unit cell and the highest density of hexagonal holes, offering more adsorption sites.

To circumvent the stability issues of borophene synthesis process, hydrogenation of borophene has been proposed theoretically.[164] Borophane, as the hydrogenated counterpart of borophene, is a gapless Dirac material (Fig. 9d).[136] Based on DFT calculations, the borophane with the maximum Li content is $Li_{0.445}B_2H_2$. Shukla and coworkers found that the diffusion barrier of Li ion on bilayer is much lower than that on hydrogen boride single layer.[165] Although borophane can be an attractive anode for LIBs, only complete hydrogenation of borophene can achieve a stable structure. Besides, introducing metal elements to provide extra electrons to π-orbitals has also been proved to be an effective way to overcome the limitation of kinetic instability of borophane.[166] Zhou's group systematically investigated the feasibility of BeB_2 and MgB_2 monolayers as anode materials for Li ion batteries.[167] The BeB_2 and MgB_2 monolayers exhibit great dynamical and thermodynamical stability. During the lithiation/delithiation process, the maximum percentage changes of the lattice parameters of the Li–BeB_2 and Li–MgB_2 systems are as low as −1.66% and 1.75%, which further prove their good cycle stability.

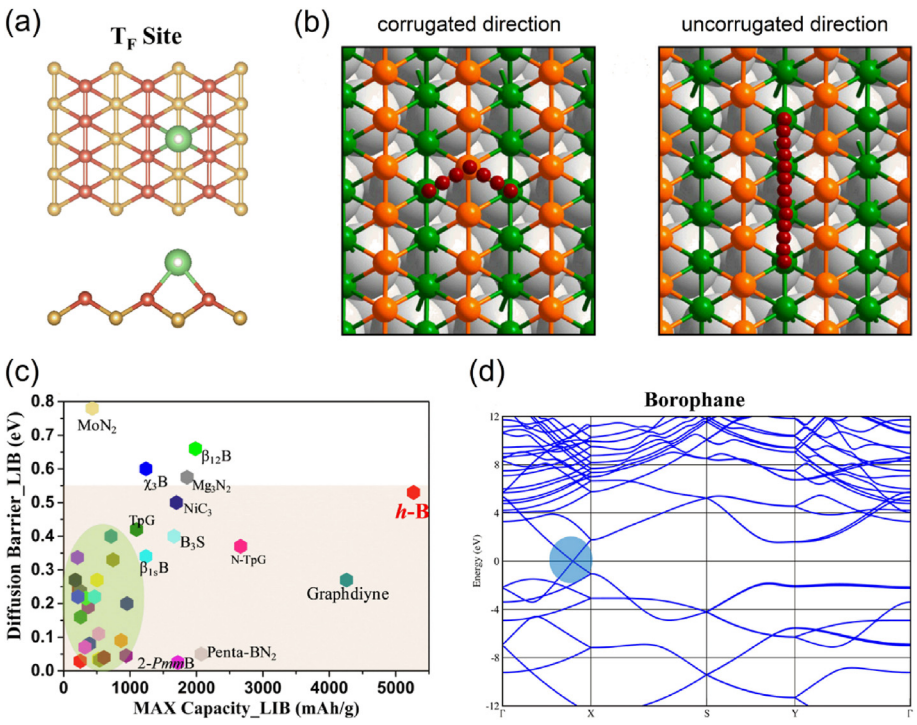

Fig. 9. (a) Top and side views of high-symmetry Li adsorption T_F site in borophene. Reproduced with permission from Ref. 131. (b) Two possible pathways of Li diffusion along corrugated (path-x) and uncorrugated (path-y) directions of the borophene layer fabricated on an Ag (111) surface. Reproduced with permission from Ref. 92. (c) DFT calculated diffusion barriers and the maximum storage capacities of h-borophene and other typical 2D anode materials for LIB. Reproduced with permission from Ref. 135. (d) Band structures of borophane. Reproduced with permission from Ref. 136.

Meanwhile, the storage capacities of Li atoms on the BeB_2 and MgB_2 monolayers can reach 1749.8 and 1750.9 mA h g^{-1}.

4.2.2. *Phosphorene*

2D phosphorene was first isolated in 2014 by Liu and coworkers through mechanical exfoliation method.[168,169] It consists of single layers of the artificially made layered black phosphorus and exhibits a unique puckered structure with sp^3 hybrid. The following two unique characters of phosphorene make it a promising anode material for Li-ion battery: (1) nonzero fundamental band gap which can be modulated by Li atoms; (2) puckered structure which can expose more surface area for Li adsorption.[170–172]

Zhao and coworkers used DFT calculations to investigate the adsorption and diffusion properties of Li atoms on single-layer and double-layer structures of phosphorene.[91] The results show that Li atoms bind strongly with phosphorene, especially for the double-layer phosphorene. The diffusion barriers and theoretical capacities of Li on monolayer and double-layer phosphorene are 0.76 eV and 432.79 mA h g^{-1}, 0.72 eV and 324.59 mA h g^{-1}, respectively. It is worth noting that there exists a semiconductor-to-conductor transition during the lithiation process (Fig. 10a). The diffusion properties of lithium ion on phosphorene have been further studied.[70,173] The results implied that the diffusion along the zigzag direction is highly favorable with a shallow energy barrier of 0.08 eV, while the diffusion along the armchair direction is almost prohibited (0.68 eV) (Fig. 10b). Guo et al. compared the performance of pristine and defect-containing phosphorenes.[174] They found that the defect can greatly increase the binding energy between the Li atom and the substrate by about 1 eV. More importantly, the defect opens a novel channel (between two adjacent grooves) for Li diffusion with an extremely low energy barrier of 0.13 eV (Fig. 10c). However, the diffusion barrier of Li ions along the zigzag direction increases sharply in the range from 0.17 to 0.49 eV.[175] Thus, the ultrafast migration of Li ions

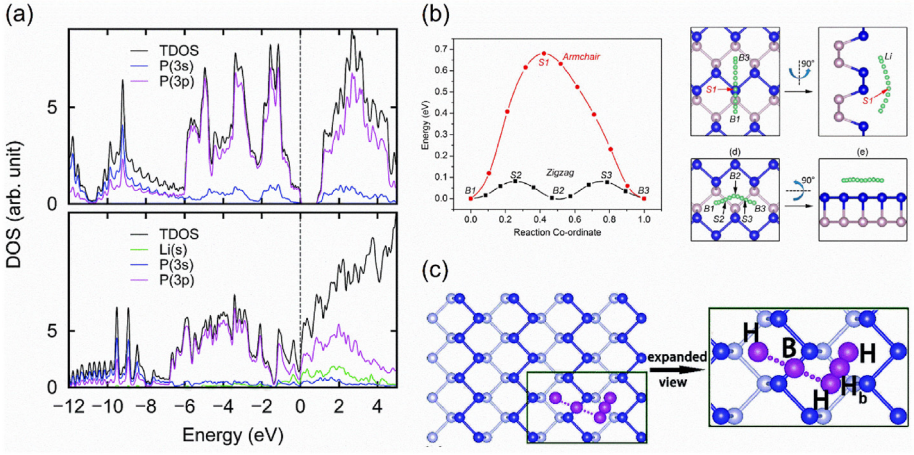

Fig. 10. (a) Total and projected density of states of the pristine phosphorene and fully lithiated phosphorene monolayers. Reproduced with permission from Ref. 91. (b) Energy profiles of Li diffusion along armchair and zigzag directions on phosphorene surface. Reproduced with permission from Ref. 70. (c) Diffusion path between two nearest H sites on phosphorene. Reproduced with permission from Ref. 174.

along the zigzag direction would be blocked by the vacancy effect. Unlike black phosphorene, 2D blue phosphorus is isotropic, and there is only one diffusion path between the nearest stable adsorption sites with an energy barrier less than 0.4 eV.[137] The blue phosphorus shows high charge capacities (865 mA h g^{-1} for single-layer and 649 mA h g^{-1} for double-layer blue phosphorus) during the lithiation process.

4.2.3. Silicene

Bulk silicon exhibits a remarkably high theoretical capacity of 4200 mA h g^{-1}, which is more than ten times of graphite (372 mA h g^{-1}).[176,177] However, the huge volume change (~400%) of silicon during lithium insertion/extraction process would cause rapid decay of Si electrode performance. In contrast to bulk phases, the associated change in 2D silicene is found to be minimal, and the possible use in LIBs has also been theoretically studied.[178]

Xu et al. found that the adsorption pattern of Li atoms on silicene changes with the concentration of Li.[138] At a very low concentration (<1.56%), Li-ions are adsorbed on hollow sites. At a high concentration, the Li chains with up-down pairs on top sites become popular (Fig. 11a). They predicted that the capacity of silicene can reach 1196 mA h g^{-1} (Table 1). Seyed-Talebi and coworkers reported that the adsorption of Li atoms turns silicene into a narrow gap semiconductor with the band gap ranging from 0.044 to 0.067 eV on different adsorption sites.[179]

Strain, defects, and heteroatom doping could greatly influence the performance of silicene in Li-ion batteries. For instance, Wang and coworkers found the tensile strain could enhance Li binding on silicene because of the increased charge transfer between Li and silicene.[180] Setiadi et al. discussed three kinds of defects (Stone-Thrower-Wales (STW), SV, and DV silicene) and found that the types of vacancy would affect the value of diffusion barrier (Fig. 11b).[181] Moreover, the diffusion barrier for the DV is much lower than the SV. Momeni and coworkers explored Li adsorption and diffusion on defective silicenes (Si-5559 and Si-5105).[182] The diffusion barriers of Li on the surface of Si-5559 and Si-5105 were calculated to be 0.24 and 0.29 eV, respectively. Based on AIMD simulations, fully lithiated Si-5559 is not stable and cannot accommodate lithium atoms (Fig. 11c). On the contrary, Si-5105 is stable and could store a certain amount of lithium atoms. The theoretical capacity of Si-5105 was calculated to be 664 mA h g^{-1}. This group also investigated the potential of heteroatom (Al-, B-, *P*-, and *N*-) doped silicenes as electrodes in Li-ion batteries.[183] They found that the adsorption energy of Li atoms on doped silicenes is larger than that on pristine silicene, and Al- and B-doped silicenes show a stronger interaction with Li than *P*- and *N*-doped silicenes, which is confirmed by the OCV results (Fig. 11d). Besides, based on the spin electronic difference plot of *N*-doped silicene, spin density is mostly concentrated around the nitrogen and three neighboring silicon atoms (Fig. 11e). For Li diffusion, doping silicene with nitrogen and phosphorus atoms facilitates the mobility of Li on the surface (diffusion barriers of 0.05 and 0.11 eV, respectively), while doping with aluminum can speed up Li diffusion in the perpendicular direction. Wu et al. designed a fluorinated penta-silicene and observed that the fluorine-concentration-induced transition from semiconductor to metal.[184] B-substituted silicenes (H–BSi_3 and *R*–BSi_3) exhibit unusual planar geometry which ensures a high theoretical capacity of 1410 mA h g^{-1} for single-layer and 846 mA h g^{-1} for double-layer BSi_3 silicenes.[185] Besides, the existence of GBs greatly improves the binding with Li, which can be ascribed to the donation of Li *2s* electron to the GBs.[186]

4.3. Metal compound

4.3.1. Transition metal sulfides

2D transition metal sulfides (TMDs) are an important class of 2D materials with the general formula of MX_2, where M denotes a transition metal and X is a chalcogen (S, Se, Te).[187–189] Among all the structures, 2H, 1 T and 1 T′ phases are considered to be the three relatively stable phases in TMD materials. Depending on the type of constituent elements and the synthesis method, one of the phases may be thermodynamically more stable than the other two.

Mo-based TMDs (such as MoS_2) as the most representative TMDs have been widely investigated as anode in Li-ion batteries. For example, 1 T-MoS_2 monolayer as the electrode has more advantages than 2H–MoS_2, since the continuous intercalation of Li ions would produce structural dissociation and induce structural transition from the 2H to the 1 T phase (Fig. 12a).[190] Based on the DFT calculations, the maximal adsorption capacity could reach 7 layers for Li on 1 T-MoS_2 monolayer with the value of 1172 mA h g^{-1}.[191] Besides, the application of tensile strain on

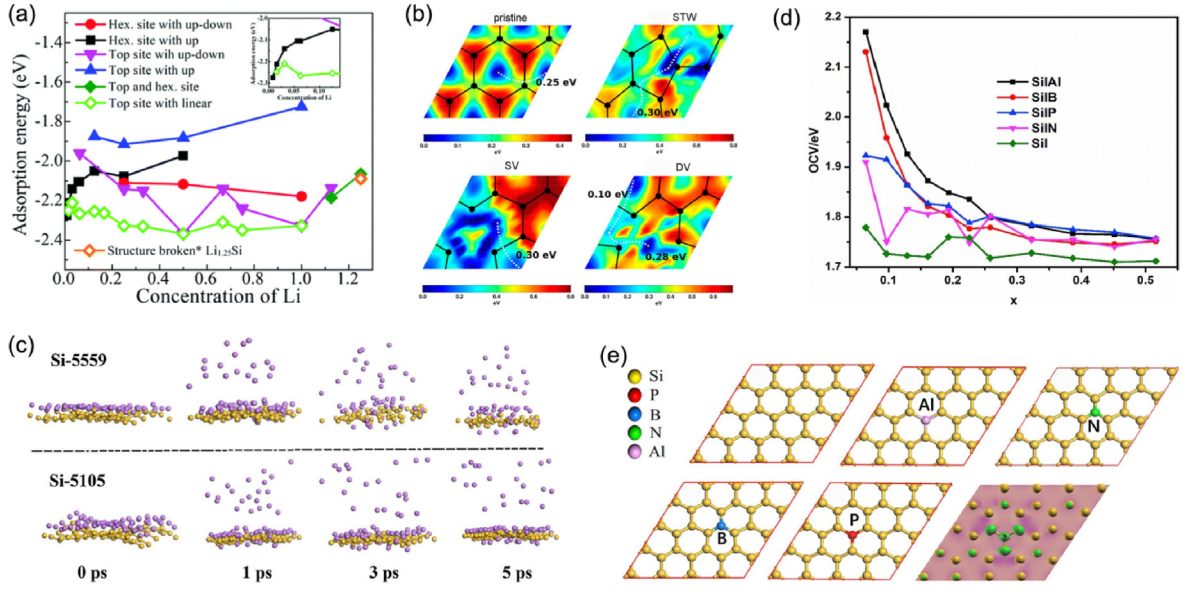

Fig. 11. (a) Adsorption energy as a function of Li concentration on silicene for different models. Reproduced with permission from Ref. 138. (b) Pseudo-color plot of energy profile of lithium diffusion on the surface of pristine, STW, SV, and DV silicene. Reproduced with permission from Ref. 181. (c) Snapshots of fully lithiated defective silicenes during AIMD simulations. Reproduced with permission from Ref. 182. (d) Variation of OCV as a function of Li concentration. (e) Optimized structure of pristine and doped silicenes, as well as spin electron density of *N*-doped silicene (the green areas show the spin densities). Reproduced with permission from Ref. 183.

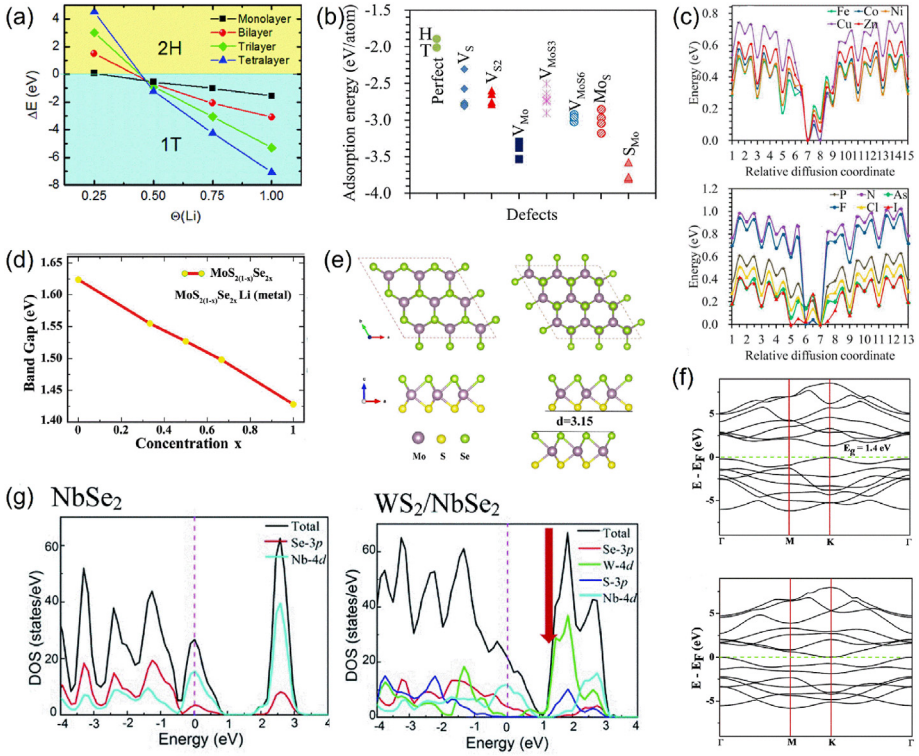

Fig. 12. (a) Energy difference (ΔE) between 2H and 1 T phases in four Li-intercalated MoS_2 nanosheets as a function of Li coverage. Reproduced with permission from Ref. 190. (b) Adsorption energies of Li adsorbed on different sites of MoS_2 around the point defect. Reproduced with permission from Ref. 192. (c) Diffusion energy profiles for Li on metal (upper) and nonmetal (lower) atom-doped monolayer MoS_2. Reproduced with permission from Ref. 193. (d) Variation of band gaps with and without lithium adsorption. Reproduced with permission from Ref. 194. (e) Top view and side view of the SLM (upper row) and DLM (lower row). Reproduced with permission from Ref. 139. (f) Band structures of WSe_2 under 0% (upper) and 10% (lower) strains. Reproduced with permission from Ref. 195. (g) Total DOS and orbital-resolved PDOS of the $NbSe_2$ monolayer and the $WS_2/NbSe_2$ heterostructure. Reproduced with permission from Ref. 142.

MoS_2 can greatly increase the adsorption energy and improve the conductivity. Compared with the pristine MoS_2, the existence of defects (including single- and few-atom vacancies, antisite, and grain boundary) on MoS_2 would enhance the adsorption energies in the range between 2.81 and 3.80 eV (Fig. 12b).[192] Sun et al. investigated the heteroatom-doping effect by substituting S with non-metal elements (N, P, As, F, Cl, and I) and Mo with metal elements (Fe, Co, Ni, Cu, and Zn) on a MoS_2 monolayer through DFT calculations.[193] The results showed that the *S*-rich or Mo-rich conditions exhibit different adsorption energies and diffusion barriers. To be specific, under the Mo-rich conditions, the substitutions of S with P, As, Cl, and I lead to negative formation energies. Under the *S*-rich conditions, the formation energies are negative only when Mo is substituted by Fe atoms. For the diffusion barrier, except Ni, Cu, and Cu dopants with energy barriers of 0.82, 0.62, and 0.72 eV, respectively, the others are around 0.25 eV (Fig. 12c). Ersan and co-workers examined the properties of lithium on the $MoS_{2(1-x)}Se_{2x}$ monolayers with different contents of x.[194] They found that the band gap of $MoS_{2(1-x)}Se_{2x}$ compounds varies with x and this semiconductor can be metalized by Li adsorption (Fig. 12d). Moreover, the penetration energy barrier for a single lithium atom to pass through the $MoS_{2(1-x)}Se_{2x}$ monolayers is large and would decrease from 2.5 to 1.3 eV with increasing selenium concentration. For Li-ion on the single-layer MoSSe (SLM) and the double-layer MoSSe (DLM) (Fig. 12e), Li-ions can be stored by both systems due to their intrinsic dipole moment and charge redistribution.[139] The theoretical capacity of the SLM is higher than that of the DLM, which are 776.5 and 452.9 mA h g^{-1}, respectively.

Except for the typical Mo-based TMDs, other TMDs also exhibit great potential as electrodes for Li-ion batteries. For example, VS_2 monolayer has been predicted to have a high theoretical capacity of 466 mA h g^{-1} and a low average open-circuit voltage of 0.93 V (vs Li/Li^+).[140] Pristine ReS_2 has been found to show a strong binding with Li atoms with an adsorption energy of −2.28 eV.[141] Strain-engineered WSe_2 monolayer shows decreased band gap from 1.4 eV to 0.7 eV after being imposed 10% tensile strain (Fig. 12f).[195] Moreover, the TMD/TMD double-layered heterostructures also exhibit excellent performance as an electrode material. Liu et al. systematically investigated the performance of WS_2, $NbSe_2$, and $WS_2/NbSe_2$ heterostructure as electrodes in Li-ion batteries.[142] They found that new electronic state occupation appear in the heterostructure, which enhances the conductivity of the system (Fig. 12g). Moreover, the Li diffusion barrier on the $WS_2/NbSe_2$ heterostructure is 0.18 eV, which is much lower than that on single WS_2 and $NbSe_2$ monolayers. Most importantly, the heterostructure was predicted to have a desirable theoretical specific capacity of 842.4 mA h g^{-1}. Wang et al. investigated the properties of MX_2 (M = Mo, W; X = S, Se) single-layer and double-layered heterostructures by the first-principles calculations.[196] They found that the heterostructures, such as MoS_2/WS_2 and $MoS_2/MoSe_2$, can increase the Li binding energy to 2.1 eV, compared with 1.4–1.8 eV for the monolayer MoX_2.

4.3.2. *MXenes*

Since the first discovery of $Ti_3C_2T_x$ in 2011, transition metal carbides and nitrides (MXenes) have attracted widespread interest.[197,198] The general formula of MXenes is $M_{n+1}X_nT_x$ (n = 1–3), where M represents the transition metal (such as Ti), X refers to carbon and/or nitrogen, and T stands for the surface terminations (for example, –O, –F, or –OH). Similar to TMDs, MXenes have been predicted to have both 1 T and 2H phase by DFT calculations. However, only 1 T phases have been experimentally prepared. It is worth mentioning that all the investigated MXenes show metallic properties which are beneficial for their application as energy storage materials.

***Ti-based MXene*:** Titanium-based MXenes (such as Ti_2C, Ti_3C_2, Ti_2CT_x, and $Ti_3C_2T_x$), as the most representative MXene materials, have attracted several computational investigations on its electronic properties and Li storage capability.

Tang and coworkers found that the bare Ti_3C_2 monolayer shows magnetic metal characters which is beneficial for enhancing the electronic conductivities (Fig. 13a).[143] Moreover, because of the low diffusion barrier (0.07 eV), Li atoms can easily transport on the surfaces of Ti_3C_2 monolayers. Er et al. observed that the adsorption energies of Li atoms on Ti_3C_2 monolayer depend on the coverage, and predicted that the capacity of Ti_3C_2 is 447.8 mA h g^{-1}.[89] Xie et al. focused on the $Ti_3C_2O_2Li_2$ system and calculated the corresponding electron localization

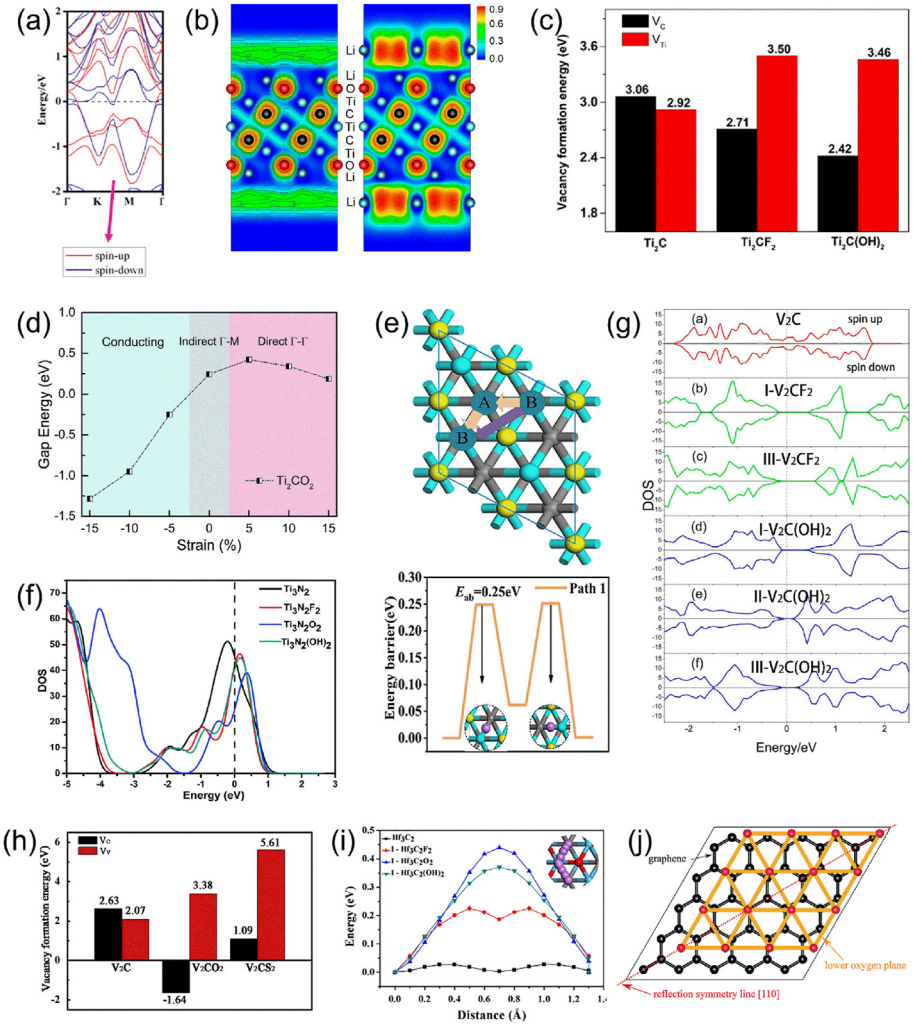

Fig. 13. (a) Band structures near the Fermi level for the Ti_3C_2 monolayer. Reproduced with permission from Ref. 143. (b) Valence ELF of (110) sections of lithiated $Ti_3C_2O_2Li_2$ monolayer and that with an extra Li layer. Reproduced with permission from Ref. 199. (c) Vacancy formation energies of Ti_2C and Ti_2CT_2 (T = F and OH) monolayers. Reproduced with permission from Ref. 200. (d) Strain dependence of band gap energy for Ti_2CO_2. Reproduced with permission from Ref. 202. (e) Schematic illustration of the Li-ion migration path on $Ti_3C_2O_2$ and the corresponding energy profiles. Reproduced with permission from Ref. 144. (f) Total DOS of Ti_3N_2, $Ti_3N_2F_2$, $Ti_3N_2O_2$ and Ti_3N_2 $(OH)_2$. The Fermi levels are set to zero and are indicated by the dashed lines. Reproduced with permission from Ref. 203. (g) Spin-resolved total DOS of V_2C, I-V_2CF_2, III-V_2CF_2, I-$V_2C(OH)_2$, II-$V_2C(OH)_2$, and III-$V_2C(OH)_2$. The Fermi levels are set to zero. Reproduced with permission from Ref. 147. (h) Vacancy formation energy for V_2C, V_2CO_2 and V_2CS_2 monolayer. Reproduced with permission from Ref. 204. (i) Diffusion barrier profiles of Li atom on Hf_3C_2 and I-$Hf_3C_2T_2$ (T = F, O, OH) monolayers. Reproduced with permission from Ref. 152. (j) M_2CX_2/graphene heterostructure in its ground state stacking. Reproduced with permission from Ref. 205.

function (ELF) plot (Fig. 13b), in which the electron transfer between Li and O and that between Ti and C can be visualized, and the interaction between two extra Li layers indicates the ability of binding an extra layer.[199] The effect of vacancies on Ti_2C and Ti_2CT_2 monolayers have been studied by Wan et al.[200] For the carbon vacancy (V_C), the surface is suggested to be modified with –OH groups (Fig. 13c). For the titanium vacancies (V_{Ti}), all the functional groups are suggested to be removed. Si-doped Ti_2C nanosheets can better satisfy the capacity demand of energy storage for lithium-ion batteries compared with pristine Ti_2C. The Si-doped Ti_2C exhibited a storage capacity of 439.4 mA h g^{-1} which nearly increased by 32% than pristine Ti_2C.[201] Strain engineering could tailor the conduction behavior.[202] The indirect band gap in pristine Ti_2CO_2 changes to a direct band gap under tensile strain and turns to close under compressive strain (Fig. 13d). Chalcogenated-$Ti_3C_2X_2$ (X = O, S, Se, and Te) MXene has been systematically investigated as anode in Li-ion batteries.[144] Among these four systems, $Ti_3C_2S_2$ exhibits enhanced Li-ion storage with a capacity of 462.6 mA h g^{-1} and a low diffusion energy barrier of 0.25 eV (Fig. 13e). Moreover, chalcogenation yields expanded interlayer spacing, which improves the Li-ion accessibility in $Ti_3C_2X_2$.

Nitride MXenes, owing to the high electrical conductivities, have also attracted intensive attention. For example, Ti_2N monolayer as electrode has a high OCV of 0.53 V, a large specific capacity of 487 mA h g^{-1}, and an extremely low diffusion barrier of 21.5 meV.[145] Yu et al. discussed the electronic properties and storage capabilities of Ti_3N_2 and $Ti_3N_2X_2$ (X = O, F, and OH) monolayers as anode materials in rechargeable batteries.[203] Both bare and terminated Ti_3N_2 monolayers exhibit metallic behavior before and after Li-ion adsorption (Fig. 13f). The existence of functional groups, except for $Ti_3N_2O_2$, is proven to be unfavorable to metal ion migration and will decrease the corresponding storage capacities. Chen and coworkers use DFT calculations to systematically discuss the mechanism of Li adsorption and diffusion on Ti_3CN and Ti_3CNT_2 (T = F, O, and OH) monolayers.[146] Based on their results, the diffusion barrier of Li ions on bare Ti_3CN is extremely low (less than 0.03 eV), and the barrier increases a lot after the introduction of surface groups (as high as 0.24–0.26 eV). It is worth noting that Li atoms prefer to be adsorbed on the nitrogen side for Ti_3CN without functional groups and the carbon side for Ti_3CN with functional groups.

***V-based MXene*:** Vanadium carbides have been predicted to exhibit excellent properties such as fast charge-discharge and high theoretical storage capacity. Fan et al. revealed that the diffusion barrier for Li on V_3C_2 is 0.04 eV and the storage capacity can reach up to 606.42 mA h g^{-1}.[74] Hu et al. performed DFT calculations to study the properties of V_2C and its F/OH functionalized derivatives.[147] The V_2C monolayer is an antiferromagnetic metal, while V_2CF_2 and $V_2C(OH)_2$ are antiferromagnetic semiconductors with a small gap (Fig. 13g). Moreover, the bare V_2C monolayer shows a very high Li storage capacity (~940 mA h g^{-1}), while the functional groups on its surface largely reduce the Li storage capacity. V_2CO_2 and V_2CS_2 exhibit larger absorption energy and lower diffusion barrier than V_2CF_2 or $V_2C(OH)_2$ monolayer.[206] Li et al. found that the diffusion barrier for Li-ion on V_2CS_2 is lower than that of O-functionalized.[204] Moreover, the presence of atomic

vanadium vacancy on V_2CS_2 monolayer exerts more prominent effects on enhancing adsorption strength than that of carbon vacancy for Li-ion (Fig. 13h). Besides, V_4C_3 monolayer exhibits excellent rate ability with the energy barriers as low as 0.048 eV for Li ions diffusion along its surface.[207]

***Other MXenes*:** Except for Ti-based and V-based MXenes, other kinds of MXenes are also widely explored by researchers. Mo_2C was predicted to be an appealing anode material because of the high storage capacity of 526 mA h g^{-1} and small diffusion barriers of 43 meV.[148,208] For Mn_2C sheet, Li atoms exhibit strong binding effect with adsorption energy of −1.93 eV, which implies high theoretical capacity (879 mA h g^{-1}).[149] The diffusion barriers of Sc_2C monolayer are as low as 0.018 eV for Li, which illustrates the high mobility and cycling ability.[150] Bare Nb_2C has shown better performance than Nb_2CX_2 (X = O, F, OH) monolayers.[151] A similar phenomenon has been found on Hf-based MXenes (Hf_3C_2, its derivatives, and hybrid passivated).[152] Bare Hf_3C_2 monolayer exhibits the lowest diffusion energy barrier of 0.027 eV for Li (Fig. 13i) and the highest theoretical capacity of 1034.70 mA h g^{-1} among all of the Hf-based MXenes. Xie et al. discussed the Li-ion storage capacities of a series of 2D MXenes (Sc_2C, Ti_2C, Ti_3C_2, V_2C, Cr_2C, and Nb_2C).[199] They recommended that the O-terminated or bare MXenes with light atomic mass (Sc, Ti, V and Cr) are more suitable as electrodes. Zhu et al. found that using S groups to replace O/F/OH functional groups could improve electric conductivities and cycling rates for Zr-based MXenes in Li-ion batteries.[209] Wu and coworkers systematically discussed the influence of a single vacancy in the M_2C (M = Sc, Ti, V, Zr, Nb, Mo, Hf, Ta, W) MXene.[210] They found that vacancy of M atom in MXene is easy to form with the formation energy ranging from 0.96 to 2.85 eV, and the vacancy defect can enhance the adsorption of Li. Aierken et al. combined graphene with six members of the MXene monolayers (M_2CX_2, where M = Sc, Ti, V, and X = OH, O) (Fig. 13j)[205] and found two promising heterostructures for Li intercalation: Ti_2CO_2/graphene and V_2CO_2/graphene. These two monolayers exhibit large binding energies of 1.43 eV per Li atom for Ti_2CO_2/graphene and 1.78 eV per Li atom for V_2CO_2/graphene when fully loaded with Li atoms, yet the interlayer friction is small. The electrochemical performances of double-metal MXenes, TiNbC and $TiNbCT_2$, as anode materials for LIBs, have also been studied.[153] Based on the results, TiNbC and $TiNbCO_2$ monolayers are predicted to be excellent anode materials for LIBs with the theoretical Li-ion storage capacity up to 351 mA h g^{-1} on TiNbC monolayer and 290 mA h g^{-1} on $TiNbCO_2$ monolayer, while $TiNbC(OH)_2$ is unstable for the adsorption of lithium and $TiNbCF_2$ is unfavorable due to the formation of ring structure between F-groups and Li-ions. For nitride MXenes, Cr_2N monolayer is not suitable for direct use as an electrode material due to its strong chemical interaction with Li ions, while its derivatives (Cr_2NF_2 and Cr_2NO_2 monolayers) are promising candidates for LIB electrodes.[211] The theoretical specific capacities of Cr_2NF_2 and Cr_2NO_2 monolayers are predicted to be 583 and 556 mA h g^{-1}, respectively.

4.3.3. *Other metal componds*

In the above discussion, the advantages of MXenes as LIB electrodes have been presented. However, the stability of MXenes will be challenged when it is exposed to water or air. In fact, 2D metal carbides (MCs) and 2D metal nitrides (MNs), as a new class of materials, have shown excellent performance in terms of stability. In addition, it is worth to note the possible carbon/nitrogen to metal ratio in this kind of materials. For instance, Xu et al. used a global-structure search method to predict two stable 2D carbide structural isomers, VC_2-α and VC_2-β monolayers (Fig. 14a).[154] These two systems show the same large theoretical capacity of 1073 mA h g^{-1}, but the diffusion barrier of Li^+ on VC_2-β monolayer is much lower than that on VC_2-α monolayer. Zhang et al. proved that MoN_2 monolayer can be exfoliated from its bulk counterpart and is suitable for a LIB cathode.[83] Both the pristine and doped MoN_2 are metallic, and Li atoms possess moderate/low migration barriers on MoN_2, which imply the good charge-discharge rates as battery electrodes. The capacity of MoN_2 monolayer is predicted to be 432 mA h g^{-1}. Zhu et al. identified an entirely planar NiC_3 monolayer as a highly symmetric anode material.[155] The NiC_3 monolayer is metallic and has antiferromagnetic ground state. The calculated diffusion barrier is 0.50 eV for Li (Fig. 14b), and the storage capacity reaches up to 1698 mA h g^{-1}. Yu and coworkers used the unbiased structural search calculations to discuss the potential of 2D Mo_xC_y structures as anodes for LIBs.[212] They found that both MoC and MoC_2 monolayers exhibit excellent electrode performances (Fig. 14c). In particular, the MoC_2 monolayer exhibits a high theoretical storage capacity of 893.5 mA h g^{-1} and a small diffusion energy barrier of 0.13 eV.

Metal phosphides as anodes for LIBs have attracted the attention of researchers due to their high average voltage as well as high gravimetric capacity (ranging from 500 to 2000 mA h g^{-1}).[213–216] Harper et al. combined four different crystal structure searching techniques on copper phosphide to screen 42 systems that met the stability criteria from about 20,000 test structures, four of which (CuP_{10}, Cu_2P_7, CuP_2 and Cu_3P) have already been reported experimentally.[217] Based on the calculation results, the Cu_2P phase is strongly suggested to be experimentally synthesized and predicted to have a theoretical gravimetric capacity of 508 mA h g^{-1} as a Li-ion battery electrode, which is greater than both Cu_3P (363 mA h g^{-1}) and graphite (372 mA h g^{-1}). It is worth noting that the actual capacities of the electrode depend on the experimental preparation method. For example, the powdered Cu_3P anodes show an initial capacity ranging from 272 mA h g^{-1} by using high-temperature synthesis

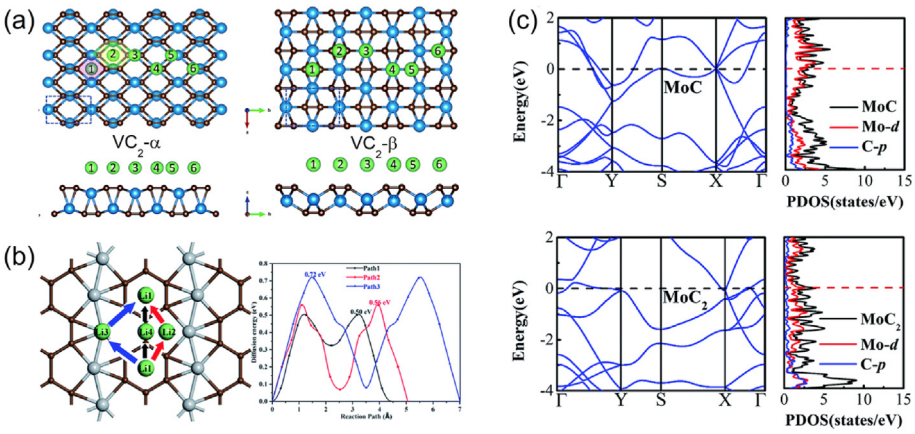

Fig. 14. (a) Structures of VC_2-α and VC_2-β. Reproduced with permission from Ref. 154. (b) Proposed Li ion migration pathways on the NiC_3 monolayer and the corresponding diffusion energy barriers. Reproduced with permission from Ref. 155. (c) Calculated band structures and projected DOS (PDOS) for MoC and MoC_2. Reproduced with permission from Ref. 212.

in a silica tube to 527 mA h g^{-1} using low-temperature solvothermal synthesis.[218] Besides, Li and coworkers found that layered GeP anode for LIBs exhibit the best performances among all Ge-based anode materials studied.[219] According to the first-principles calculations, the initial layered crystal structure of GeP can be reconstructed during charging due to its low formation energy, thus providing significant reversibility during cycling. This unique healing phenomenon may be an important reason for the large capacity of lithium storage.

In general, 2D materials possess many unique advantages and exhibit excellent performance (conductivity, capacity, and multiplication capability) as anode for Li-ion batteries. However, cell performance depends not only on the inherent properties of the anode material, but also on the crystallinity or amorphous structure of the anode material as well as the shape, size, and component state. Thus, a rational design of the crude material is more beneficial for its practical application during charging and discharging. Here, we propose two possible future directions for advanced 2D anode compounds. First, the development of co-doping techniques remains crucial to the exploitation of the synergistic effects of different heteroatom doping. The second is to use the hierarchical structure of 2D nanomaterials to create interconnected conduction channels for facilitated Li-ion transfer.

5. Two-dimensional electrode materials for Li–S batteries

The charging and discharging process of Li–S batteries is a complex electrochemical process. It can be divided into four stages according to the phase change of sulfur substances. First, lithium metal reacts with sulfur (S_8) to produce long-chain soluble Li_2S_8. After further reaction of the dissolved Li_2S_8 and lithium, the long-chain Li_2S_8 is reduced into low-order Li_2S_4, accompanied by steeply declined battery voltage and a gradual increase in solution viscosity. Then, with the occurrence of the two-phase liquid-solid reduction reaction, the low-order dissolved Li_2S_4 is transformed to insoluble Li_2S_2 or Li_2S. The last stage involves a solid-solid reduction from the insoluble Li_2S_2 to Li_2S. In fact, the dissolution of lithium polysulfide (LiPS) intermediates in liquid electrolyte would trigger a shuttle process, which is detrimental to the electrode and may cause a significant decline in capacity. 2D materials possess the following two unique advantages which could potentially solve the problems mentioned above. On the one hand, 2D materials have uniform and tunable exposed lattice planes which provide LiPSs with sufficient reactive sites, depressing the shuttle problem. On the other hand, the unique morphology of some 2D materials, such as the pore-like structure of carbon-based materials, can offer a large free space for high S loading and volume buffering, improving the safety performance. Therefore, anchoring polysulfides within the cathode have proven to be an effective approach to designing high-performance Li–S batteries.[38]

Graphene and its derivatives have found numerous applications in Li–S battery, because of their large specific area, high electrical conductivity, and mechanical stabilities.[220,221] For instance, *N*-doped graphene (NG) is one of the most promising anchoring materials, because the N dopant induces chemical interaction in carbon-based materials and promotes reactivity compared with pure carbon materials. Yin et al. carried out a systematic study of the interactions between LiPSs and NG with different doping configurations (including isolated/clustered amino, graphitic, pyridinic, and pyrrolic *N*-dopants) (Fig. 15a).[222] They found that the clustered pyridinic *N*-dopants in NG exhibit a much stronger binding ability to LiPSs than others, implying that the clustered pyridinic *N*-dopants in NG are effective immobilizers of soluble LiPSs. This can be explained by that pyrrolic N can form the coordination bond of LiN_3 with Li_2S_n.[223] However, too strong interactions would cause the decomposition of molecules.[224] To solve this problem, Yi et al. proposed a LiNG model, which is an optimized structure of Li-trapping on pyridinic NG.[225] The results showed that the trapped Li atoms interact with S atoms in a LiPS molecule to form a Li–S bond and result in a decreased binding energy always larger than the binding energies of LiPS with DOL or DME. Thus, the LiNG effectively prevents the dissolution of LiPS into the electrolyte and avoids the structural decomposition of the LiPS molecule. Other heteroatom doped 2D carbon nanosheets are also beneficial for the performance of Li–S batteries. Wasalathilake et al. studied the interactions between bare or oxygen-containing functional graphene (hydroxyl, epoxy, and carboxyl groups) and sulfur (S_8) or long-chain lithium polysulfides (Li_2S_8 and Li_2S_4).[226] During the initial unlithiated stage, the interaction between sulfur and bare graphene or oxygen-containing functional graphene (OFG) is nearly the same and is dominated by van der Waals attraction. During the lithiation stage, functional groups significantly enhance the interaction with Li_2S_8/Li_2S_4 by forming a coordinate covalent Li–O bond. Hou et al. performed a systematical study of various heteroatom (including B, N, O, F, P, S, and Cl) doped nanocarbon materials.[227] Based on the calculation results of binding energy (Fig. 15b), the N/O-doped graphene nanoribbons (GNRs)

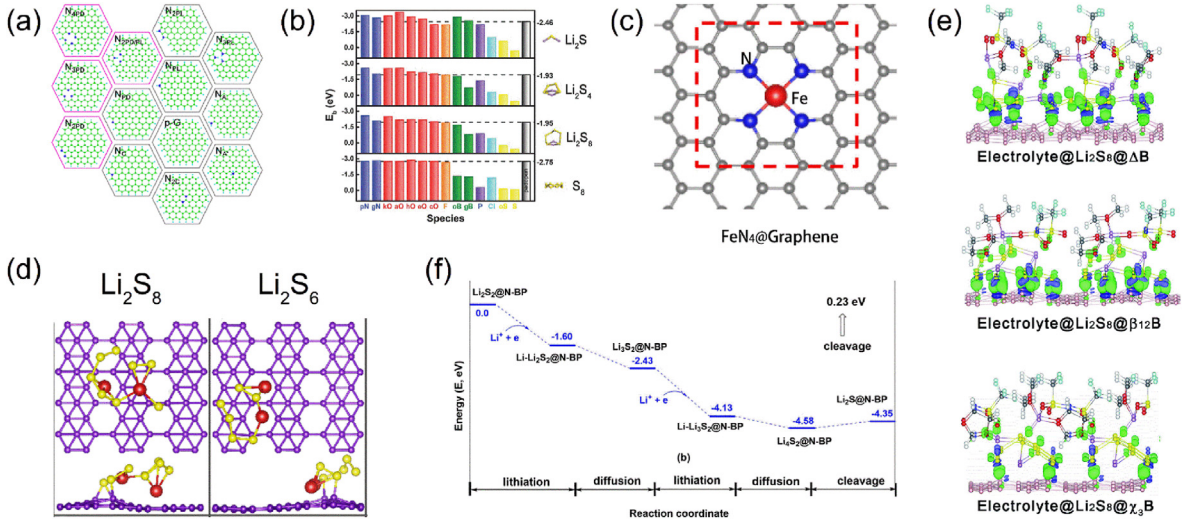

Fig. 15. (a) Structural diagrams of p-G and *N*-G with different doping configurations. Reproduced with permission from Ref. 222. (b) Binding energy of Li_2S, Li_2S_4, Li_2S_8, and S_8 interacting with X-doped GNRs and undoped G. Reproduced with permission from Ref. 227. (c) Top view of fully optimized structure of the iron and nitrogen co-doped graphene surface. Reproduced with permission from Ref. 229. (d) Top and side views of Li_2S_8-β_{12}-borophene and Li_2S_6-β_{12}-borophene systems. Reproduced with permission from Ref. 79. (e) Charge density differences of Li_2S_8 on borophenes with electrolytes (DOL and DME). Reproduced with permission from Ref. 237. (f) Energy profiles for Li_2S_2 → Li_2S conversion on *N*-BP surfaces. Reproduced with permission from Ref. 238.

can trap soluble intermediates better than undoped GNR because of the dipole-dipole electrostatic interaction, thus greatly improve the capacity and Coulombic efficiency. Hybridization of graphene with more than one inorganic material is also considered as an effective approach to improving the rate capability and cycling stability. Li and coworkers designed B and N co-doped graphene sheets through substituting one N dopant with a B atom.[228] Due to the synergistic contribution of *N*–Li and B–S interactions, the polysulfide diffusion is found to be effectively retarded in G–B–N-pyrrolic and G–B–N-hex systems. Zhang and coworkers revealed that iron and nitrogen co-doped graphene monolayer is a good anchoring material because of the unique ring structure of four-membered (Li–S–Fe–N) (Fig. 15c), which not only ensures the stability of adsorption structure but also improves the catalytic effect.[229] Except for iron element, other transition metals also exhibit very good anchoring and catalytic effects.[230–233] Recently, Zeng et al. systematically investigated a series of graphene-supported transition metal SACs (from 3 d, 4 d, and 5 d) for application in Li–S batteries to deepen the understanding of the Li_2S oxidation and SRR processes.[234] The MoN_4@G and WN_4@G were screened out as optimal catalysts for catalyzing Li_2S oxidation with the energy barrier E_b values of 0.58 and 0.55 eV, respectively, as well as competitive trapping capability and reduction activity. For defective graphene, Kaghazchi's group found the defect sites cannot improve too much the ability of graphene to catch lithium polysulfides in Li–S batteries, and the performance of S cathodes in Li–S batteries will not be better on the defective graphene, which agrees with experimental results.[235] As carbon allotropes, 2D GDY-based monolayers, have also been proposed as promising anchoring materials for Li–S Batteries.[236] Sun's group used first-principle simulations to study the anchoring performance of porous triphenylene–graphdiyne (TPGDY), boron-GDY, triphenylene-GDY, and nitrogen-GDY (NGDY–$C_{18}N_6$ and NGDY–$C_{36}N_6$) monolayers.[236] All the five substrates exhibited moderate adsorption energies with Li_2S_n molecules, and the electronic conductivities of all the hosts exhibit great improvement after adsorption.

Borophene, because of the metallicities and the porous configuration, has attracted intense interest as cathodes for Li–S cells.[239] Grixti et al. used DFT to investigate the potential of β_{12}-borophene as the host material.[79] They found that the borophene has strong binding with Li_2S_n species, especially for Li_2S_8 and Li_2S_6 which show a slight structure deformation during the anchoring process (Fig. 15d). Zhao's group proposed a solution by introducing the vacancy,[240] and they found that the defective borophene exhibites moderate adsorption ability, which can maintain a balance between adsorption strength and the intactness of Li_2S_n species. Besides, the construction of the heterogeneous structure (borophene/graphene) can also restrain the deformation of borophenes.[241] Moreover, the competition between hosts and electrolytes has also been deeply discussed by Rao and coworkers.[237] The charge accumulations are mainly distributed between the S and B atoms rather than Li_2S_n and electrolyte (Fig. 15e), implying that the Li_2S_n species prefer to adsorb on borophene surfaces rather than to dissolve in electrolytes.

Phosphorene is a kind of 2D material with a unique puckered structure, whose large exposed surface area makes it a promising anchoring material for polysulfide immobilization.[169,171] Zhao et al. revealed that all the Li_2S_n species can interact with phosphorene with moderate binding energies (1.0–2.0 eV).[242] Moreover, considering the unique structure of phosphorene, Li_2S_n species exhibit small diffusion barriers in both zigzag (~0.20 eV) and armchair directions (~0.58 eV). Similar to borophene, the defective phosphorene exhibits better anchoring effect.[243] Lin et al. studied three types of defective black phosphorene (SW, SV and DV) as host materials.[244] The LiPSs on defective black phosphorene (BP) exhibit larger binding energy (1.13–3.03 eV) than those on BP (1.12–2.12 eV), suggesting that the introduction of vacancies in BP could enhance its capture ability of LiPSs. Besides, the defective phosphorene exhibits better electrical conductivity with reduced band gap, which greatly improves the rate capability.[245] The heteroatom doping of BP exhibits excellent catalytic properties. Liu's group systematically discussed the performance of polysulfide on B-doped BP, Al-doped BP, *N*-doped BP, and pristine BP.[238] They found that the Li_2S_2 to Li_2S conversion on BP surfaces undergoes lithiation-diffusion twice ($Li_2S_2 \rightarrow Li_3S_2 \rightarrow Li_4S_2$), and a final cleavage step (from Li_4S_2 to Li_2S) (Fig. 15f). For the lithiation processes, all of the systems show exergonic characters. However, for the cleavage step, BP and *N*-BP show endoergic while B-BP and Al-BP not. Therefore, B-BP and Al-BP not only promote the kinetic process but also favor the LiPS conversion.

The application of silicene in Li–S battery has also been theoretically studied. Very recently, Fan's group proposed embedding a series of 3*d* transition metals into siloxene to form single-atom catalysts (TM-SA-siloxenes) as sulfur hosts.[246] Among them, Co-SA-siloxene is identified as the optimal candidate with moderate adsorption energies for polysulfides in the range of 0.58–4.43 eV and outstanding bifunctional electrocatalytic activity for SRR and Li_2S decomposition.

Metal sulfide electrodes not only exhibit excellent conductivities but also good catalytic effects. For example, Lv and coworkers studied the interaction features between MX (M = Ge, Sn; X = S, Se) monolayers and LiPSs.[247] The MX monolayers exhibit moderate adsorption energies with LiPSs and a low diffusion barrier of Li and polysulfides. Chen et al. summarized the periodic law for the strong anchoring of polysulfides on the first-row transition-metal sulfides (TMSs).[248] They found the following three rules: (1) For TMSs, *S*-binding is more favorable than Li-binding. (2) Among the first-row TMSs, VS exhibits the highest binding energy of −4.89 eV. (3) For most of the first-row TMSs, the surface lithium diffusion barrier is less than 0.30 eV (Fig. 16a). This work deeply discussed the role of TMSs as polar sulfur hosts and provided valuable guidance to the rational design of sulfur cathode. Moreover, the design of bilayer heterostructure can be a good additive for sulfur cathodes. Fang et al. constructed a unique asymmetric polar Ti_2CO/WS_2 heterostructure to simultaneously trap LiPSs and achieve Li_2S catalytic activity.[249] The Ti_2CO-side can restrain the LiPSs effectively, and the WS_2 side possesses a lower diffusion or decomposition barrier which is good for fast electrochemical processes. Very recently, a machine learning (ML) method, which is an optimization method based on a large amount of DFT data, has been proposed to rapidly and accurately predict the binding energies of LiPS adsorbed on the surface of AB_2 structures of TMSs.[250] Zhang and coworkers selected $MoSe_2$ as a case study in this work and found that the ML method shows six orders of magnitude faster than the DFT calculation (Fig. 16b) with relatively low mean absolute error (0.1 eV) in the prediction. Besides, researchers also found the ML method can be extended to other 2D similar AB_2-typed structures (such as WSe_2) for screening the host materials and understanding the adsorption mechanisms.

Metal oxides have strong chemical anchoring abilities with polysulfides because of the strong polar surfaces induced by oxygen anions. Zhu and coworkers investigated the anchoring ability of MgO nanotubes (MgONT) and defective MgO nanotubes (MgONTv) with LiPSs by DFT.[251] Based on band gap analysis, the conductivity of MgONTv is better than MgONT with the band gap decreased from 3.33 to 1.61 eV, and the adsorption of LiPSs can further reduce the gap. Besides, based on the adsorption energies, the presence of an oxygen vacancy greatly enhances the binding strength between the hosts and the LiPSs.

Transition metal carbides and nitrides (MXenes) are good electrode materials for Li–S batteries due to their large surface areas and interlayer spaces.[253–256] Among 2D MXenes, Ti-based carbides are the most widely reported electrodes in Li–S batteries. Based on DFT calculations, the bare Ti-based MXenes cannot be directly used in Li–S batteries due to the extremely strong Ti–S interaction (Ti atoms in Ti-based MXenes and S atoms in Li_2S_n species), which would decompose the Li_2S_n species.[252,257] Thus, surface modification is required to obtain suitable adsorption strength with Li_2S_n species. For example, Zhao et al. found that Ti_2CO_2 and $Ti_3C_2O_2$ monolayers exhibit a good balance between the binding strength and intactness of the Li_2S_n species because of the Li–O bonds (Li-ions in Li_2S_n species and O atoms in Ti_2CO_2 and $Ti_3C_2O_2$ monolayer).[258] Rao et al. discussed the interactions of LiPSs on bare and surface functionalized (−F, –O, and –OH groups) Ti_2C.[257] They found that

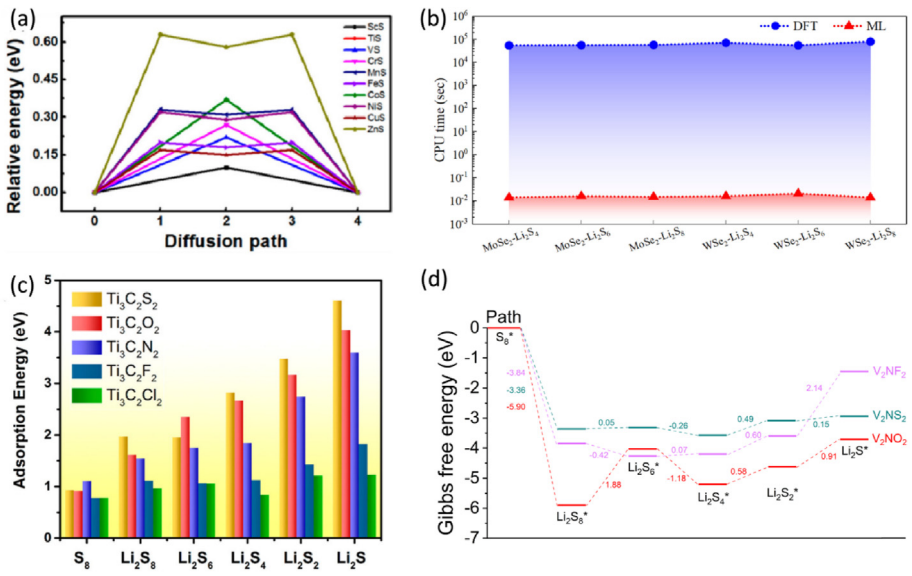

Fig. 16. (a) Energy profiles for diffusion processes of Li ion on the first-row TMSs surface. Reproduced with permission from Ref. 248. (b) Comparison of CPU computational time for $MoSe_2/WSe_2$ towards three lithium polysulfides. Reproduced with permission from Ref. 250. (c) Adsorption energies of S_8 and Li_2S_n on $Ti_3C_2T_2$. Reproduced with permission from Ref. 252. (d) Gibbs free energy profiles for the sulfur reduction reaction on V_2NO_2, V_2NF_2, and V_2NS_2. Reproduced with permission from Ref. 82.

the Li_2S_n species can maintain their molecular configurations on Ti_2CO_2 and Ti_2CF_2 monolayer. However, the long-chain Li_2S_n clusters on $Ti_2C(OH)_2$ are distorted without complete dissociation, which can be explained by the fact that OH-terminated material exhibits stronger interaction with Li_2S_n species than O-terminated and F-terminated materials. Chung and coworkers discussed the difference of the anchoring mechanisms in O and F functionalized Ti_2C MXenes.[256] They found that the effective suppression of the shuttling can be explained by the strong interaction between Ti_2CF_2 and Li_2S_n intermediates, while for Ti_2CO_2, the shuttle effect can be prevented because the soluble high-order LiPSs (Li_2S_8, Li_2S_6) prefer to be oxidized to insoluble elemental sulfur on Ti_2CO_2. Theoretical study further proved that some other functional groups, such as S and N, can also help suppress the polysulfide shuttling. Wang et al. introduced different surface terminating groups (T = N, P, O, S, F and Cl) to enhance the electrochemical performance of Ti_3C_2.[252] They found that $Ti_3C_2S_2$ and $Ti_3C_2O_2$ can achieve high performance in Li–S batteries with great anchoring strength and catalytic ability (Fig. 16c). Zhao's group drew the similar conclusion. They believed that strong Ti–S interaction can lead to stable *S*-terminated Ti_2C MXene (Ti_2CS_2) and the Ti_2CS_2 had the highest affinity to polysulfides compared with Ti_2CO_2 and Ti_2CF_2.[259] Except for the typical Ti-based MXenes, other types of MXenes have also been studied. For example, Fan's group systematically discussed the anchoring behaviors between $M_3C_2O_2$ (M = Cr, V, Ti, Nb, Hf and Zr) MXenes and lithium polysulfides.[260] They identified a monotonic relationship between the binding energy and the lattice constant, that is, $M_3C_2O_2$ MXenes with a smaller lattice constant tend to exhibit a stronger anchoring effect. Wang et al. designed a potential *S*-functionalized V_2C (V_2CS_2) MXene.[261] The results suggested that vdW interactions play a major role between soluble Li_2S_n species and V_2CS_2. Very recently, our group found that the functionalized V_2NS_2 exhibits outstanding bifunctional catalytic activities toward sulfur reduction reaction (SRR) with a low Gibbs free energy barrier of 0.49 eV (Fig. 16d).[82]

In the previous sections, we have reviewed the DFT calculations on different categories of the 2D electrode materials for Li–S batteries. In fact, there are some materials that have not been extensively studied by theoretical calculations but deserve attention. For example, Li et al. proposed a 2D copper-based MOF (Cu-BHT) as a promising sulfur host for high-performance Li–S batteries by the first-principles calculations.[262] The Cu-BHT monolayer exhibits synergistic dual interaction based on the Li−Ss bond and Sa−Cu bond (Ss: sulfur in Cu-BHT, Sa: sulfur in Li_2S_n) with a moderate interaction with LiPSs (binding energy ranging from 0.8 to 2.0 eV). Gao et al. demonstrated that the 2D hexaaminobenzene-based coordination polymers (2D-HAB-CPs) is a promising cathode material with ultrahigh energy density for Li–S batteries.[13] Through the combination of DFT calculations and global structural search code, they proved that the theoretical energy density of 2D-HAB-CP can reach 1395 W h kg^{-1}. Song and coworkers predicted that the 2D magnetic Fe_3GeX_2 (X = S, Se and Te) monolayers show bifunctional electrocatalytic activity to the S reduction reaction (SRR) and the Li_2S decomposition reaction in Li–S batteries.[263] To be specific, their calculation results showed that Gibbs free energy of SRR is as low as 0.35 eV, while the Li_2S decomposition barrier is in the range of 0.38–0.94 eV, which greatly improves the conversion efficiencies in discharging and charging processes. Moreover, the metallic features and the anchoring functionality of Fe_3GeX_2 monolayers further imply the potential of Fe_3GeX_2 in Li–S battery. This work not only provides a promising catalyst for the high-performance Li–S batteries but also gives a guide to the catalyst design.

6. Challenges and outlook of 2D electrodes for Li-ion and Li–S batteries

Albeit diverse in mechanisms, there are some common challenges concerning 2D electrodes for Li-ion and Li–S batteries.

The first one is that the bonding chemistry of the 2D electrodes in both Li-ion and Li–S batteries remains unclear. For Li-ion batteries, too weak or too strong bonding between Li-ion and substrate is not beneficial for Li adsorption or desorption on the substrates. For Li–S batteries, too weak adsorption cannot depress the shuttle effect while too strong bonding will lead to decomposition of sulfur species.[79] However, understanding of the critical boundary of the binding energy is still not sufficient in both theoretical and experimental aspects. Another challenge is the difficulties in the accurate prediction of binding energies of Li-ion and LiPSs on 2D materials, which can play an instructive role in accelerating the electrode design. Recently, Gao et al. built a predictive model for small molecule binding energies on the surface of metals and their oxides by using intrinsic surface properties such as valence and electronegativity of surface atoms,[264] and their approaches may be extended to 2D electrode design.

Secondly, although many predicted 2D materials are stable, it is still difficult to synthesize them experimentally. This is because the DFT calculations are usually used to evaluate the stability of the final product, while little attention is paid to the energy barrier from the initial reactants to the final products. Large discrepancies between the experiments and the calculations already emerge in some specific properties. For some significant parameters in experiments such as cycle number, a reasonable method to make preliminary predictions by calculations does

not exist. To bridge the gap between theoretical prediction and experiments, not only should the methods with stricter screening constraints be proposed, but also effective algorithms and theoretical descriptors are urged to develop.

The third challenge is related to the design of novel materials, where more advanced property-oriented inverse design methods need to be developed. For example, in order to facilitate the rate capability of electrodes, new materials with metallic characters are better. At the present stage, the exploration of potential electrode materials is mainly focused on the following two directions. One is to improve the performance of existing materials and expand their application ranges. The other is to design and prepare new materials with intriguing properties. Moreover, due to the limited understanding of the chemistry and physics of some newly developed 2D materials, collaborations between theorists and experimentalists are in great demand for electrode material design.

Last but not least, the concept of sustainability should be included in the framework of electrochemical storage.[265,266] When designing sustainable electrode candidates, full consideration should be given to the abundance, toxicity, and economic cost of the elements. On the other hand, to improve the overall sustainability of battery technology, there is still an urgent need for easy recycling.

From the perspective of theoretical modelling, the combination of multiscale and diverse computational methods may be a feasible way for screening potential 2D electrode materials for Li-ion and Li–S batteries. For example, Zhang et al. combined high-throughput DFT calculations with ML methods to transfer the research results of $MoSe_2$ to a similar AB_2 structure for Li–S electrode applications.[250] With the development of computing power and new approaches, we also believe that a 2D material database for Li-ion and Li–S batteries can be constructed in the near future originating from the whole 2D material database,[27,29] taking into consideration the intrinsic principles, we discussed in Section 3 and all the adsorption sites and patterns for Li-ion and LiPSs.

7. Summary

Li-ion and Li–S batteries are two very important types of batteries. For Li-ion batteries, achieving large-scale commercialization is its most eye-catching advantage. For Li–S batteries, it offers substantial increase in specific capacity and specific energy compared with Li-ion batteries. However, it still faces many unsolved problems that prevent its commercialization process.

In this review, we summarize the applications of *ab initio* simulations in Li-ion and Li–S battery materials, with a particular focus on various 2D electrode materials. Benefited from the emergence of new algorithms and new computing resources, theoretical descriptors have made significant contributions to the understanding of the intrinsic properties of battery materials and the electrochemical reaction mechanism, covering the ground state structure, adsorption site, diffusion barrier, catalytic activity, and capacity of 2D materials. It should be emphasized that although many novel 2D materials are discussed in this review, they cannot cover all the 2D systems studied so far. With the help of advanced theoretical computation and experimental techniques, we believe that batteries with higher energy density and longer cycle stability will be realized in the near future.

Declaration of competing interest

Haitao Huang is an editorial board member for *Materials Reports: Energy* and was not involved in the editorial review or the decision to publish this article. The authors declare that they are not aware of any competing financial interests or personal relationships that could influence the work reported in this paper.

Acknowledgments

This work was supported by the Research Grants Council of the Hong Kong Special Administrative Region, China (PolyU152178/20 E), the Hong Kong Polytechnic University (1-W19S), and Science and Technology Program of Guangdong Province of China (2020A0505090001).

References

1. Chen H, Cong TN, Yang W, et al. Progress in electrical energy storage system: a critical review. *Prog Nat Sci*. 2009;19:291–312.
2. Yang Y, Bremner S, Menictas C, Kay M. Battery energy storage system size determination in renewable energy systems: a review. *Renew Sustain Energy Rev*. 2018;91:109–125.
3. Martin G, Rentsch L, Höck M, Bertau M. Lithium market research-global supply, future demand and price development. *Energy Storage Mater*. 2017;6:171–179.
4. Sun Y, Liu N, Cui Y. Promises and challenges of nanomaterials for lithium-based rechargeable batteries. *Nat Energy*. 2016;1, 16071.
5. Shahjalal M, Roy PK, Shams T, et al. A review on second-life of Li-ion batteries: prospects, challenges, and issues. *Energy*. 2022;241, 122881.
6. Ji X, Nazar LF. Advances in Li-S batteries. *J Mater Chem*. 2010;20:9821–9826.
7. Rauh R, Abraham K, Pearson G, et al. A lithium/dissolved sulfur battery with an organic electrolyte. *J Electrochem Soc*. 1979;126:523.
8. Huang Y, Lin L, Zhang C, et al. Recent advances and strategies toward polysulfides shuttle inhibition for high-performance Li-S batteries. *Adv Sci*. 2022;9, 2106004.
9. Barghamadi M, Kapoor A, Wen C. A review on Li-S batteries as a high efficiency rechargeable lithium battery. *J Electrochem Soc*. 2013;160:A1256–A1263.
10. Zhou L, Danilov DL, Eichel RA, Notten PHL. Host materials anchoring polysulfides in Li-S batteries reviewed. *Adv Energy Mater*. 2020;11(15), 2001304.
11. Cheng X-B, Huang J-Q, Zhang Q. Li metal anode in working lithium-sulfur batteries. *J Electrochem Soc*. 2017;165:A6058.
12. Fotouhi A, Auger DJ, O'Neill L, et al. Lithium-sulfur battery technology readiness and applications-a review. *Energies*. 2017;10:1937.
13. Gao G, Zheng F, Pan F, Wang L-W. Theoretical investigation of 2D conductive microporous coordination polymers as Li-S battery cathode with ultrahigh energy density. *Adv Energy Mater*. 2018;8, 1801823.
14. Liu D, Zhang C, Zhou G, et al. Catalytic effects in lithium-sulfur batteries: promoted sulfur transformation and reduced shuttle effect. *Adv Sci*. 2018;5, 1700270.
15. Xu R, Zou X, Liu B, Cheng H-M. Computational design and property predictions for two-dimensional nanostructures. *Mater Today*. 2018;21:391–418.
16. Tan C, Cao X, Wu X-J, et al. Recent advances in ultrathin two-dimensional nanomaterials. *Chem Rev*. 2017;117:6225–6331.
17. Ladha DG. A review on density functional theory-based study on two-dimensional materials used in batteries. *Mater Today Chem*. 2019;11:94–111.
18. Peng L, Zhu Y, Chen D, et al. Two-dimensional materials for beyond-lithium-ion batteries. *Adv Energy Mater*. 2016;6, 1600025.
19. Bahari Y, Mortazavi B, Rajabpour A, et al. Application of two-dimensional materials as anodes for rechargeable metal-ion batteries: a comprehensive perspective from density functional theory simulations. *Energy Storage Mater*. 2021;35:203–282.
20. Lin J, Yu T, Han F, Yang G. Computational predictions of two-dimensional anode materials of metal-ion batteries. *Wiley Interdiscip Rev Comput Mol Sci*. 2020;10(5): e1473.
21. He Q, Yu B, Li Z, Zhao Y. Density functional theory for battery materials. *Energy Environ. Mater*. 2019;2:264–279.
22. Liu Y, Guo B, Zou X, et al. Machine learning assisted materials design and discovery for rechargeable batteries. *Energy Storage Mater*. 2020;31:434–450.
23. Lei YJ, Liu HW, Yang Z, et al. A review on the status and challenges of cathodes in room-temperature Na-S batteries. *Adv Funct Mater*. 2023;33(11), 2212600.
24. Chen M, Liu Y, Zhang Y, et al. Lithium-rich sulfide/selenide cathodes for next-generation lithium-ion batteries: challenges and perspectives. *Chem Commun*. 2022; 58:3591–3600.
25. Kohn W, Sham LJ. Self-consistent equations including exchange and correlation effects. *Phys Rev*. 1965;140:A1133.
26. Tan C, Cao X, Wu XJ, et al. Recent advances in ultrathin two-dimensional nanomaterials. *Chem Rev*. 2017;117:6225–6331.
27. Haastrup S, Strange M, Pandey M, et al. The computational 2D materials database: high-throughput modeling and discovery of atomically thin crystals. *2D Mater*. 2018;5, 042002.
28. Schleder GR, Padilha AC, Acosta CM, et al. From DFT to machine learning: recent approaches to materials science-a review. *J Phys: Materials*. 2019;2, 032001.
29. Ashton M, Paul J, Sinnott SB, Hennig RG. Topology-scaling identification of layered solids and stable exfoliated 2D materials. *Phys Rev Lett*. 2017;118, 106101.
30. Choudhary K, Kalish I, Beams R, Tavazza F. High-throughput identification and characterization of two-dimensional materials using density functional theory. *Sci Rep*. 2017;7:1–16.
31. Yang E, Ji H, Jung Y. Two-dimensional transition metal dichalcogenide monolayers as promising sodium ion battery anodes. *J Phys Chem C*. 2015;119:26374–26380.
32. Mounet N, Gibertini M, Schwaller P, et al. Two-dimensional materials from high-throughput computational exfoliation of experimentally known compounds. *Nat Nanotechnol*. 2018;13:246–252.
33. Ying Y, Fan K, Luo X, Huang H. Predicting two-dimensional pentagonal transition metal monophosphides for efficient electrocatalytic nitrogen reduction. *J Mater Chem A*. 2019;7:11444–11451.
34. Ying Y, Fan K, Zhu S, et al. Theoretical investigation of monolayer RhTeCl semiconductors as photocatalysts for water splitting. *J Phys Chem C*. 2020;124: 639–646.

35. Ying Y, Lin Z, Huang H. "Edge/basal plane half-reaction separation" mechanism of two-dimensional materials for photocatalytic water splitting. *ACS Energy Lett*. 2023; 8:1416–1423.
36. Guan J, Liu D, Zhu Z, Tománek D. Two-dimensional phosphorus carbide: competition between sp2 and sp3 bonding. *Nano Lett*. 2016;16:3247–3252.
37. Tan WC, Cai Y, Ng RJ, et al. Few-layer black phosphorus carbide field-effect transistor via carbon doping. *Adv Mater*. 2017;29, 1700503.
38. Fan K, Huang H. Two-dimensional host materials for lithium-sulfur batteries: a review and perspective. *Energy Storage Mater*. 2022;50:696–717.
39. Fan K. *Theoretical Investigation of Two-Dimensional Materials as Promising Electrode Materials for Li-Ion and Li-S Batteries*. Dissertations, Hong Kong Polytechnic University; 2022.
40. Shulenburger L, Baczewski AD, Zhu Z, et al. The nature of the interlayer interaction in bulk and few-layer phosphorus. *Nano Lett*. 2015;15:8170–8175.
41. Jung JH, Park C-H, Ihm J. A rigorous method of calculating exfoliation energies from first principles. *Nano Lett*. 2018;18:2759–2765.
42. An Y, Hou Y, Gong S, et al. Evaluating the exfoliation of two-dimensional materials with a Green's function surface model. *Phys Rev B*. 2020;101, 075416.
43. Björkman T, Gulans A, Krasheninnikov AV, Nieminen RM. van der Waals bonding in layered compounds from advanced density-functional first-principles calculations. *Phys Rev Lett*. 2012;108, 235502.
44. Mostaani E, Drummond N, Fal'Ko V. Quantum Monte Carlo calculation of the binding energy of bilayer graphene. *Phys Rev Lett*. 2015;115, 115501.
45. Sansone G, Maschio L, Usvyat D, et al. Toward an accurate estimate of the exfoliation energy of black phosphorus: a periodic quantum chemical approach. *J Phys Chem Lett*. 2016;7:131–136.
46. Zhou J, Gao S, Guo Z, Sun Z. Ti-enhanced exfoliation of V_2AlC into V_2C MXene for lithium-ion battery anodes. *Ceram Int*. 2017;43:11450–11454.
47. Nolan AM, Zhu Y, He X, et al. Computation-accelerated design of materials and interfaces for all-solid-state lithium-ion batteries. *Joule*. 2018;2:2016–2046.
48. Yu T, Zhang S, Li F, et al. Stable and metallic two-dimensional TaC_2 as an anode material for lithium-ion battery. *J Mater Chem*. 2017;5:18698–18706.
49. Ishikawa T, Miyake T. Evolutionary construction of a formation-energy convex hull: practical scheme and application to a carbon-hydrogen binary system. *Phys Rev B*. 2020;101, 214106.
50. Anelli A, Engel EA, Pickard CJ, Ceriotti M. Generalized convex hull construction for materials discovery. *Phy. Rev. Mater*. 2018;2, 103804.
51. Glass CW, Oganov AR, Hansen N. USPEX—evolutionary crystal structure prediction. *Comput Phys Commun*. 2006;175:713–720.
52. Lyakhov AO, Oganov AR, Stokes HT, Zhu Q. New developments in evolutionary structure prediction algorithm USPEX. *Comput Phys Commun*. 2013;184: 1172–1182.
53. Wang Y, Lv J, Zhu L, Ma Y, Calypso. A method for crystal structure prediction. *Comput Phys Commun*. 2012;183:2063–2070.
54. Wang Y, Lv J, Zhu L, et al. Materials discovery via CALYPSO methodology. *J Phys Condens Matter*. 2015;27, 203203.
55. Liborio L, Sturniolo S, Jochym D. Computational prediction of muon stopping sites using ab initio random structure searching (AIRSS). *J Chem Phys*. 2018;148, 134114.
56. Togo A, Tanaka I. First principles phonon calculations in materials science. *Scripta Mater*. 2015;108:1–5.
57. Giannozzi P, De Gironcoli S, Pavone P, Baroni S. Ab initio calculation of phonon dispersions in semiconductors. *Phys Rev B*. 1991;43:7231.
58. Kaur K, Murali D, Nanda B. Stretchable and dynamically stable promising two-dimensional thermoelectric materials: ScP and ScAs. *J Mater Chem*. 2019;7: 12604–12615.
59. Fan K, Ying Y, Luo X, Huang H. Monolayer PC_5/PC_6: promising anode materials for lithium-ion batteries. *Phys Chem Chem Phys*. 2020;22:16665–16671.
60. Malyi OI, Sopiha KV, Persson C. Energy, phonon, and dynamic stability criteria of two-dimensional materials. *ACS Appl Mater Interfaces*. 2019;11:24876–24884.
61. van Gog H, Li W-F, Fang C, et al. Thermal stability and electronic and magnetic properties of atomically thin 2D transition metal oxides. *NPJ 2D Mate. Appl*. 2019;3: 1–12.
62. Pastore G, Smargiassi E, Buda F. Theory of ab initio molecular-dynamics calculations. *Phys Rev*. 1991;44:6334.
63. Grotendorst J. *Modern Methods and Algorithms of Quantum Chemistry*. NIC; 2000.
64. Li F, Fan K, Tian Y, et al. General flux-free synthesis of single crystal Ni-rich layered cathodes by employing a Li-containing spinel transition phase for lithium-ion batteries. *J Mater Chem A*. 2022;10:16420–16429.
65. He X, Zhu Y, Epstein A, Mo Y. Statistical variances of diffusional properties from ab initio molecular dynamics simulations. *npj Comput Mater*. 2018;4:1–9.
66. Danuta H, Juliusz U. *Electric Dry Cells and Storage Batteries*. Google Patents; 1962.
67. Yuan L-D, Deng H-X, Li S-S, et al. Unified theory of direct or indirect band-gap nature of conventional semiconductors. *Phys Rev B*. 2018;98, 245203.
68. Kumar A, Ahluwalia P. Electronic structure of transition metal dichalcogenides monolayers 1H-MX_2 (M= Mo, W; X= S, Se, Te) from ab-initio theory: new direct band gap semiconductors. *Eur Phys J B*. 2012;85:1–7.
69. Splendiani A, Sun L, Zhang Y, et al. Emerging photoluminescence in monolayer MoS_2. *Nano Lett*. 2010;10:1271–1275.
70. Li W, Yang Y, Zhang G, Zhang Y-W. Ultrafast and directional diffusion of lithium in phosphorene for high-performance lithium-ion battery. *Nano Lett*. 2015;15: 1691–1697.
71. Xiao B, Li Y-C, Yu X-F, Cheng J-B. Penta-graphene: A promising anode material as the Li/Na-ion battery with both extremely high theoretical capacity and fast charge/discharge rate. *ACS Appl Mater Interfaces*. 2016;8:35342–35352.
72. Li N, Meng Q, Zhu X, et al. Lattice constant-dependent anchoring effect of MXenes for lithium-sulfur (Li-S) batteries: a DFT study. *Nanoscale*. 2019;11:8485–8493.
73. Johnson PA, Bartolotti LJ, Ayers PW, et al. *Charge Density and Chemical Reactions: A Unified View from Conceptual DFT, Modern Charge-density Analysis*. Netherlands: Springer; 2011:715–764.
74. Fan K, Ying Y, Li X, et al. Theoretical investigation of V_3C_2 MXene as prospective high-capacity anode material for metal-ion (Li, Na, K, and Ca) batteries. *J Phys Chem C*. 2019;123:18207–18214.
75. Tang W, Chill S, Henkelman G. *Bader Charge Analysis*. The Univeristy of Texas and Austin; 1970.
76. Olivier JP. Modeling physical adsorption on porous and nonporous solids using density functional theory. *J Porous Mater*. 1995;2:9–17.
77. Hammer B, Hansen LB, Nørskov JK. Improved adsorption energetics within density-functional theory using revised Perdew-Burke-Ernzerhof functionals. *Phys Rev B*. 1999;59:7413.
78. Ruiz VG, Liu W, Zojer E, et al. Density-functional theory with screened van der Waals interactions for the modeling of hybrid inorganic-organic systems. *Phys Rev Lett*. 2012;108, 146103.
79. Grixti S, Mukherjee S, Singh CV. Two-dimensional boron as an impressive lithium-sulphur battery cathode material. *Energy Storage Mater*. 2018;13:80–87.
80. Xiao Z, Li Z, Li P, et al. Ultrafine Ti_3C_2 MXene nanodots-interspersed nanosheet for high-energy-density lithium-sulfur batteries. *ACS Nano*. 2019;13:3608–3617.
81. Hensley AJ, Ghale K, Rieg C, et al. DFT-based method for more accurate adsorption energies: an adaptive sum of energies from RPBE and vdW density functionals. *J Phys Chem C*. 2017;121:4937–4945.
82. Fan K, Ying Y, Luo X, Huang H. Nitride MXenes as sulfur hosts for thermodynamic and kinetic suppression of polysulfide shuttling: a computational study. *J Mater Chem A*. 2021;9:25391–25398.
83. Zhang X, Yu Z, Wang S-S, et al. Theoretical prediction of Mon_2 monolayer as a high capacity electrode material for metal ion batteries. *J Mater Chem*. 2016;4: 15224–15231.
84. Er D, Li J, Naguib M, et al. Ti_3C_2 MXene as a high capacity electrode material for metal (Li, Na, K, Ca) ion batteries. *ACS Appl Mater Interfaces*. 2014;6:11173–11179.
85. Lee S, Kim J, Lee J, Cho BH. State-of-charge and capacity estimation of lithium-ion battery using a new open-circuit voltage versus state-of-charge. *J Power Sources*. 2008;185:1367–1373.
86. Snihir I, Rey W, Verbitskiy E, et al. Battery open-circuit voltage estimation by a method of statistical analysis. *J Power Sources*. 2006;159:1484–1487.
87. Urban A, Seo D-H, Ceder G. Computational understanding of Li-ion batteries. *npj Comput Mater*. 2016;2:1–13.
88. Ge B, Chen B, Li L. Ternary transition metal chalcogenides Ti_2PX_2 (X= S, Se, Te) anodes for high performance metal-ion batteries: a DFT study. *Appl Surf Sci*. 2021; 550, 149177.
89. Er D, Li J, Naguib M, et al. Ti_3C_2 MXene as a high capacity electrode material for metal (Li, Na, K, Ca) ion batteries. *ACS Appl Mater Interfaces*. 2014;6:11173–11179.
90. Henkelman G, Jónsson H. Improved tangent estimate in the nudged elastic band method for finding minimum energy paths and saddle points. *J Chem Phys*. 2000; 113:9978–9985.
91. Zhao S, Kang W, Xue J. The potential application of phosphorene as an anode material in Li-ion batteries. *J Mater Chem*. 2014;2:19046–19052.
92. Zhang Y, Wu Z-F, Gao P-F, et al. Could borophene be used as a promising anode material for high-performance lithium ion battery? *ACS Appl Mater Interfaces*. 2016; 8:22175–22181.
93. Henkelman G, Uberuaga BP, Jónsson H. A climbing image nudged elastic band method for finding saddle points and minimum energy paths. *J Chem Phys*. 2000; 113:9901–9904.
94. Wert C, Zener C. Interstitial atomic diffusion coefficients. *Phys Rev*. 1949;76:1169.
95. Vineyard GH. Frequency factors and isotope effects in solid state rate processes. *J Phys Chem Solid*. 1957;3:121–127.
96. Jensen F. Activation energies and the Arrhenius equation. *Qual Reliab Eng Int*. 1985; 1:13–17.
97. Ertel K, Carstensen J. Examination of a modified Arrhenius relationship for pharmaceutical stability prediction. *Int J Pharm*. 1990;61:9–14.
98. Mo Y, Ong SP, Ceder G. First principles study of the $Li_{10}GeP_2S_{12}$ lithium super ionic conductor material. *Chem Mater*. 2012;24:15–17.
99. Kamaya N, Homma K, Yamakawa Y, et al. A lithium superionic conductor. *Nat Mater*. 2011;10:682–686.
100. Weber DA, Senyshyn A, Weldert KS, et al. Structural insights and 3D diffusion pathways within the lithium superionic conductor $Li_{10}GeP_2S_{12}$. *Chem Mater*. 2016; 28:5905–5915.
101. Carlson J, Gandolfi S, Pederiva F, et al. Quantum Monte Carlo methods for nuclear physics. *Rev Mod Phys*. 2015;87:1067.
102. Wu Q, He B, Song T, et al. Cluster expansion method and its application in computational materials science. *Comput Mater Sci*. 2016;125:243–254.
103. Sanchez J, Mohri T. Approximate solutions to the cluster variation free energies by the variable basis cluster expansion. *Comput Mater Sci*. 2016;122:301–306.
104. Van De Walle A, Asta M, Ceder G. The alloy theoretic automated toolkit: a user guide. *Calphad*. 2002;26:539–553.
105. van de Walle A, Ceder G. Automating first-principles phase diagram calculations. *J Phase Equil*. 2002;23:348–359.
106. Marzari N, Mostofi AA, Yates JR, et al. Maximally localized Wannier functions: theory and applications. *Rev Mod Phys*. 2012;84:1419.
107. Van der Ven A, Ceder G, Asta M, Tepesch P. First-principles theory of ionic diffusion with nondilute carriers. *Phys Rev B*. 2001;64, 184307.
108. Novoselov KS, Geim AK, Morozov SV, et al. Electric field effect in atomically thin carbon films. *Science*. 2004;306:666–669.

109. Lee E, Persson KA. Li absorption and intercalation in single layer graphene and few layer graphene by first principles. *Nano Lett.* 2012;12:4624–4628.
110. Pollak E, Geng B, Jeon K-J, et al. The interaction of Li^+ with single-layer and few-layer graphene. *Nano Lett.* 2010;10:3386–3388.
111. Fan X, Zheng W, Kuo J-L, Singh DJ. Adsorption of single Li and the formation of small Li clusters on graphene for the anode of lithium-ion batteries. *ACS Appl Mater Interfaces*. 2013;5:7793–7797.
112. Liu M, Kutana A, Liu Y, Yakobson BI. First-principles studies of Li nucleation on graphene. *J Phys Chem Lett*. 2014;5:1225–1229.
113. Datta D, Li J, Koratkar N, Shenoy VB. Enhanced lithiation in defective graphene. *Carbon*. 2014;80:305–310.
114. Sun C, Searles DJ. Lithium storage on graphdiyne predicted by DFT calculations. *J Phys Chem C*. 2012;116:26222–26226.
115. Yu Y-X, Graphenylene. A promising anode material for lithium-ion batteries with high mobility and storage. *J Mater Chem.* 2013;1:13559–13566.
116. Zhang Q, Tang C, Zhu W, Cheng C. Strain-enhanced Li storage and diffusion on the graphyne as the anode material in the Li-ion battery. *J Phys Chem C*. 2018;122:22838–22848.
117. Makaremi M, Mortazavi B, Singh CV. Carbon ene-yne graphyne monolayer as an outstanding anode material for Li/Na ion batteries. *Appl Mater Today*. 2018;10:115–121.
118. Li X, Wang Q, Jena P. ψ-Graphene: a new metallic allotrope of planar carbon with potential applications as anode materials for lithium-ion batteries. *J Phys Chem Lett.* 2017;8:3234–3241.
119. Thomas S, Lee CH, Jana S, et al. Phographene as a high-performance anode material with high specific capacity and fast Li diffusion: from structural, electronic, and mechanical properties to LIB applications. *J Phys Chem C*. 2019;123:21345–21352.
120. Zhang X, Jin L, Dai X, et al. A record-high ion storage capacity of T-graphene as two-dimensional anode material for Li-ion and Na-ion batteries. *Appl Surf Sci*. 2020;527,146849.
121. Wu D, Yang B, Chen H, Ruckenstein E. Nitrogenated holey graphene C_2N monolayer anodes for lithium-and sodium-ion batteries with high performance. *Energy Storage Mater*. 2019;16:574–580.
122. Kong X. Metal-free Si-doped graphene: a new and enhanced anode material for Li ion battery. *J Alloys Compd*. 2016;687:534–540.
123. Hu J, Ouyang C, Yang SA, Yang HY. Germagraphene as a promising anode material for lithium-ion batteries predicted from first-principles calculations. *Nanoscale Horiz*. 2019;4:457–463.
124. Denis PA. Lithium adsorption on heteroatom mono and dual doped graphene. *Chem Phys Lett*. 2017;672:70–79.
125. Fan X, Zheng W, Kuo J-L. Adsorption and diffusion of Li on pristine and defective graphene. *ACS Appl Mater Interfaces*. 2012;4:2432–2438.
126. Okamoto Y. Density functional theory calculations of lithium adsorption and insertion to defect-free and defective graphene. *J Phys Chem C*. 2016;120:14009–14014.
127. Hardikar RP, Das D, Han SS, et al. Boron doped defective graphene as a potential anode material for Li-ion batteries. *Phys Chem Chem Phys*. 2014;16:16502–16508.
128. Zhou L-J, Hou Z, Wu L-M, Zhang Y-F. First-principles studies of lithium adsorption and diffusion on graphene with grain boundaries. *J Phys Chem C*. 2014;118:28055–28062.
129. Thomas S, Nam EB, Lee SU. Atomistic dynamics investigation of the thermomechanical properties and Li diffusion kinetics in ψ-graphene for LIB anode material. *ACS Appl Mater Interfaces*. 2018;10:36240–36248.
130. Hu J, Liu Y, Liu N, et al. Theoretical prediction of T-graphene as a promising alkali-ion battery anode offering ultrahigh capacity. *Phys Chem Chem Phys*. 2020;22:3281–3289.
131. Jiang H, Lu Z, Wu M, et al. Borophene: a promising anode material offering high specific capacity and high rate capability for lithium-ion batteries. *Nano Energy*. 2016;23:97–104.
132. Zhang X, Hu J, Cheng Y, et al. Borophene as an extremely high capacity electrode material for Li-ion and Na-ion batteries. *Nanoscale*. 2016;8:15340–15347.
133. Huang T, Tian B, Guo J, et al. Semiconducting borophene as a promising anode material for Li-ion and Na-ion batteries. *Mater Sci Semicond Process*. 2019;89:250–255.
134. Jiang N, Li B, Ning F, Xia D. All boron-based 2D material as anode material in Li-ion batteries. *J Energy Chem*. 2018;27:1651–1654.
135. Li J, Tritsaris GA, Zhang X, et al. Monolayer honeycomb borophene: a promising anode material with a record capacity for lithium-ion and sodium-ion batteries. *J Electrochem Soc*. 2020;167, 090527.
136. Jena NK, Araujo RB, Shukla V, Ahuja R. Borophane as a benchmate of graphene: a potential 2D material for anode of Li and Na-ion batteries. *ACS Appl Mater Interfaces*. 2017;9:16148–16158.
137. Li Q-F, Duan C-G, Wan X, Kuo J-L. Theoretical prediction of anode materials in Li-ion batteries on layered black and blue phosphorus. *J Phys Chem C*. 2015;119:8662–8670.
138. Xu S, Fan X, Liu J, et al. Adsorption of Li on single-layer silicene for anodes of Li-ion batteries. *Phys Chem Chem Phys*. 2018;20:8887–8896.
139. Shang C, Lei X, Hou B, et al. Theoretical prediction of Janus MoSSe as a potential anode material for lithium-ion batteries. *J Phys Chem C*. 2018;122:23899–23909.
140. Jing Y, Zhou Z, Cabrera CR, Chen Z. Metallic VS_2 monolayer: a promising 2D anode material for lithium ion batteries. *J Phys Chem C*. 2013;117:25409–25413.
141. Mukherjee S, Banwait A, Grixti S, et al. Adsorption and diffusion of lithium and sodium on defective rhenium disulfide: a first principles study. *ACS Appl Mater Interfaces*. 2018;10:5373–5384.
142. Liu H, Huang Z, Wu G, et al. A novel $WS_2/NbSe_2$ vdW heterostructure as an ultrafast charging and discharging anode material for lithium-ion batteries. *J Mater Chem*. 2018;6:17040–17048.
143. Tang Q, Zhou Z, Shen P. Are MXenes promising anode materials for Li ion batteries? Computational studies on electronic properties and Li storage capability of Ti_3C_2 and $Ti_3C_2X_2$ (X= F, OH) monolayer. *J Am Chem Soc*. 2012;134:16909–16916.
144. Li D, Chen X, Xiang P, et al. Chalcogenated-$Ti_3C_2X_2$ MXene (X= O, S, Se and Te) as a high-performance anode material for Li-ion batteries. *Appl Surf Sci*. 2020;501,144221.
145. Pan H. Electronic properties and lithium storage capacities of two-dimensional transition-metal nitride monolayers. *J Mater Chem*. 2015;3:21486–21493.
146. Chen X, Kong Z, Li N, et al. Proposing the prospects of Ti_3CN transition metal carbides (MXenes) as anodes of Li-ion batteries: a DFT study. *Phys Chem Chem Phys*. 2016;18:32937–32943.
147. Hu J, Xu B, Ouyang C, et al. Investigations on V_2C and V_2CX_2 (X= F, OH) monolayer as a promising anode material for Li ion batteries from first-principles calculations. *J Phys Chem C*. 2014;118:24274–24281.
148. Sun Q, Dai Y, Ma Y, et al. Ab initio prediction and characterization of Mo_2C monolayer as anodes for lithium-ion and sodium-ion batteries. *J Phys Chem Lett*. 2016;7:937–943.
149. Zhou Y, Zu X. Mn_2C sheet as an electrode material for lithium-ion battery: a first-principles prediction. *Electrochim Acta*. 2017;235:167–174.
150. Lv X, Wei W, Sun Q, et al. Sc_2C as a promising anode material with high mobility and capacity: a first-principles study. *ChemPhysChem*. 2017;18:1627–1634.
151. Zhu J, Chroneos A, Schwingenschlögl U. Nb-based MXenes for Li-ion battery applications. *Phys Status Solidi Rapid Res Lett*. 2015;9:726–729.
152. Yang Z, Zheng Y, Li W, Zhang J. Investigation of two-dimensional Hf-based MXenes as the anode materials for Li/Na-ion batteries: a DFT study. *J Comput Chem*. 2019;40:1352–1359.
153. Li Y-M, Chen W-G, Guo Y-L, Jiao Z-Y. Theoretical investigations of TiNbC MXenes as anode materials for Li-ion batteries. *J Alloys Compd*. 2019;778:53–60.
154. Xu J, Wang D, Lian R, et al. Structural prediction and multilayer Li^+ storage in two-dimensional VC_2 carbide studied by first-principles calculations. *J Mater Chem*. 2019;7:8873–8881.
155. Zhu C, Qu X, Zhang M, et al. Planar NiC_3 as a reversible anode material with high storage capacity for lithium-ion and sodium-ion batteries. *J Mater Chem*. 2019;7:13356–13363.
156. Ogitsu T, Schwegler E, Galli G. β-Rhombohedral boron: at the crossroads of the chemistry of boron and the physics of frustration. *Chem Rev*. 2013;113:3425–3449.
157. Tang H, Ismail-Beigi S. Novel precursors for boron nanotubes: the competition of two-center and three-center bonding in boron sheets. *Phys Rev Lett*. 2007;99,115501.
158. Wu X, Dai J, Zhao Y, et al. Two-dimensional boron monolayer sheets. *ACS Nano*. 2012;6:7443–7453.
159. Mannix AJ, Zhou X-F, Kiraly B, et al. Synthesis of borophenes: anisotropic, two-dimensional boron polymorphs. *Science*. 2015;350:1513–1516.
160. Ma F, Jiao Y, Gao G, et al. Graphene-like two-dimensional ionic boron with double Dirac cones at ambient condition. *Nano Lett*. 2016;16:3022–3028.
161. Liu H, Gao J, Zhao J. From boron cluster to two-dimensional boron sheet on Cu (111) surface: growth mechanism and hole formation. *Sci Rep*. 2013;3:3238.
162. Liu Y, Penev ES, Yakobson BI. Probing the synthesis of two-dimensional boron by first-principles computations. *Angew Chem Int Ed*. 2013;52:3156–3159.
163. Feng B, Zhang J, Zhong Q, et al. Experimental realization of two-dimensional boron sheets. *Nat Chem*. 2016;8:563–568.
164. Makaremi M, Mortazavi B, Singh CV. 2D hydrogenated graphene-like borophene as a high capacity anode material for improved Li/Na ion batteries: a first principles study. *Mater Today Energy*. 2018;8:22–28.
165. Shukla V, Araujo RB, Jena NK, Ahuja R. Borophene's tryst with stability: exploring 2D hydrogen boride as an electrode for rechargeable batteries. *Phys Chem Chem Phys*. 2018;20:22008–22016.
166. Zhang C, Jiao Y, Ma F, et al. Predicting a graphene-like WB_4 nanosheet with a double Dirac cone, an ultra-high Fermi velocity and significant gap opening by spin-orbit coupling. *Phys Chem Chem Phys*. 2017;19:5449–5453.
167. Wan M, Zhao S, Zhang Z, Zhou N. Two-dimensional BeB_2 and MgB_2 as high capacity Dirac anodes for li-ion batteries: a DFT Study. *J Phys Chem C*. 2022;126:9642–9651.
168. Bridgman P. Two new modifications of phosphorus. *J Am Chem Soc*. 1914;36:1344–1363.
169. Brent JR, Savjani N, Lewis EA, et al. Production of few-layer phosphorene by liquid exfoliation of black phosphorus. *Chem Commun*. 2014;50:13338–13341.
170. Liu H, Neal AT, Zhu Z, et al. Phosphorene: an unexplored 2D semiconductor with a high hole mobility. *ACS Nano*. 2014;8:4033–4041.
171. Carvalho A, Wang M, Zhu X, et al. Phosphorene: from theory to applications. *Nat Rev Mater*. 2016;1:1–16.
172. Hu T, Hong J. First-principles study of metal adatom adsorption on black phosphorene. *J Phys Chem C*. 2015;119:8199–8207.
173. Yao Q, Huang C, Yuan Y, et al. Theoretical prediction of phosphorene and nanoribbons as fast-charging Li ion battery anode materials. *J Phys Chem C*. 2015;119:6923–6928.
174. Guo G-C, Wei X-L, Wang D, et al. Pristine and defect-containing phosphorene as promising anode materials for rechargeable Li batteries. *J Mater Chem*. 2015;3:11246–11252.
175. Zhang R, Wu X, Yang J. Blockage of ultrafast and directional diffusion of Li atoms on phosphorene with intrinsic defects. *Nanoscale*. 2016;8:4001–4006.
176. Ma D, Cao Z, Hu A. Si-based anode materials for Li-ion batteries: a mini review. *Nano-Micro Lett*. 2014;6:347–358.

177. Du Z, Zhang S, Liu Y, et al. Facile fabrication of reticular polypyrrole-silicon core-shell nanofibers for high performance lithium storage. *J Mater Chem*. 2012;22:11636–11641.
178. Aufray B, Kara A, Vizzini S, et al. Graphene-like silicon nanoribbons on Ag (110): a possible formation of silicene. *Appl Phys Lett*. 2010;96, 183102.
179. Seyed-Talebi SM, Kazeminezhad I, Beheshtian J. Theoretical prediction of silicene as a new candidate for the anode of lithium-ion batteries. *Phys Chem Chem Phys*. 2015;17:29689–29696.
180. Wang X, Luo Y, Yan T, et al. Strain enhanced lithium adsorption and diffusion on silicene. *Phys Chem Chem Phys*. 2017;19:6563–6568.
181. Setiadi J, Arnold MD, Ford MJ. Li-ion adsorption and diffusion on two-dimensional silicon with defects: a first principles study. *ACS Appl Mater Interfaces*. 2013;5:10690–10695.
182. Momeni MJ, Chowdhury C, Mousavi-Khoshdel M. Density functional theory study of defective silicenes as anode materials for lithium ion batteries. *J Mol Graph Model*. 2017;78:206–212.
183. Momeni MJ, Mousavi-Khoshdel M, Targholi E. First-principles investigation of adsorption and diffusion of Li on doped silicenes: prospective materials for lithium-ion batteries. *Mater Chem Phys*. 2017;192:125–130.
184. Wu D, Wang S, Zhang S, et al. Stabilization of two-dimensional penta-silicene for flexible lithium-ion battery anodes via surface chemistry reconfiguration. *Phys Chem Chem Phys*. 2019;21:1029–1037.
185. Tan X, Cabrera CR, Chen Z. Metallic BSi_3 silicene: a promising high capacity anode material for lithium-ion batteries. *J Phys Chem C*. 2014;118:25836–25843.
186. Wang X, Liu H, Huttula M, et al. First-principles studies of lithium adsorption and diffusion on silicene with grain boundaries. *Int J Quant Chem*. 2019;119, e25913.
187. Manzeli S, Ovchinnikov D, Pasquier D, et al. 2D transition metal dichalcogenides. *Nat Rev Mater*. 2017;2:1–15.
188. Chhowalla M, Shin HS, Eda G, et al. The chemistry of two-dimensional layered transition metal dichalcogenide nanosheets. *Nat Chem*. 2013;5:263–275.
189. Ding W, Hu L, Dai J, et al. Highly ambient-stable 1T-MoS_2 and 1T-WS_2 by hydrothermal synthesis under high magnetic fields. *ACS Nano*. 2019;13:1694–1702.
190. Shu H, Li F, Hu C, et al. The capacity fading mechanism and improvement of cycling stability in MoS_2-based anode materials for lithium-ion batteries. *Nanoscale*. 2016;8:2918–2926.
191. He X, Wang R, Yin H, et al. 1T-MoS_2 monolayer as a promising anode material for (Li/Na/Mg)-ion batteries. *Appl Surf Sci*. 2022;584, 152537.
192. Sun X, Wang Z, Fu YQ. Defect-mediated lithium adsorption and diffusion on monolayer molybdenum disulfide. *Sci Rep*. 2015;5:1–9.
193. Sun X, Wang Z. Adsorption and diffusion of lithium on heteroatom-doped monolayer molybdenum disulfide. *Appl Surf Sci*. 2018;455:911–918.
194. Ersan F, Gökoğlu G k, Aktürk E. Adsorption and diffusion of lithium on monolayer transition metal dichalcogenides ($MoS_{2(1-x)}Se_{2x}$) alloys. *J Phys Chem C*. 2015;119:28648–28653.
195. Rehman J, Ali R, Ahmad N, et al. Theoretical investigation of strain-engineered WSe_2 monolayers as anode material for Li-ion batteries. *J Alloys Compd*. 2019;804:370–375.
196. Wang D, Liu L-M, Zhao S-J, et al. Potential application of metal dichalcogenides double-layered heterostructures as anode materials for Li-ion batteries. *J Phys Chem C*. 2016;120:4779–4788.
197. Anasori B, Lukatskaya MR, Gogotsi Y. 2D metal carbides and nitrides (MXenes) for energy storage. *Nat Rev Mater*. 2017;2, 16098.
198. Anasori B, Xie Y, Beidaghi M, et al. Two-dimensional, ordered, double transition metals carbides (MXenes). *ACS Nano*. 2015;9:9507–9516.
199. Xie Y, Naguib M, Mochalin VN, et al. Role of surface structure on Li-ion energy storage capacity of two-dimensional transition-metal carbides. *J Am Chem Soc*. 2014;136:6385–6394.
200. Wan Q, Li S, Liu J-B. First-principle study of Li-ion storage of functionalized Ti_2C monolayer with vacancies. *ACS Appl Mater Interfaces*. 2018;10:6369–6377.
201. Das S, Shamim SUD, Hossain MK, et al. A novel silicon-doped 2D Ti_2C MXene monolayer as high capacity stable anode material for lithium ion batteries: Insight from density functional theory study. *Appl Surf Sci*. 2022;600, 154173.
202. Li Y, Li N, Zhao S, et al. Strain-tunable electronic properties and lithium storage of 2D transition metal carbide (MXene) Ti_2CO_2 as a flexible electrode. *J Mater Chem*. 2020;8:760–769.
203. Yu H, Lin W, Zhang Y, et al. Exploring the potentials of Ti_3N_2 and $Ti_3N_2X_2$ (X= O, F, OH) monolayers as anodes for Li or non-Li ion batteries from first-principles calculations. *RSC Adv*. 2019;9:40340–40347.
204. Li Y-M, Guo Y-L, Jiao Z-Y. The effect of S-functionalized and vacancies on V_2C MXenes as anode materials for Na-ion and Li-ion batteries. *Curr Appl Phys*. 2020;20:310–319.
205. Aierken Y, Sevik C, Gülseren O, et al. MXenes/graphene heterostructures for Li battery applications: a first principles study. *J Mater Chem*. 2018;6:2337–2345.
206. Yan B, Lu C, Zhang P, et al. Oxygen/sulfur decorated 2D MXene V_2C for promising lithium ion battery anodes. *Mater Today Commun*. 2020;22, 100713.
207. Peng Q, Rehman J, Eid K, et al. Vanadium carbide (V_4C_3) MXene as an efficient anode for Li-ion and Na-ion batteries. *Nanomaterials*. 2022;12:2825.
208. Çakır D, Sevik C, Gülseren O, Peeters FM. Mo_2C as a high capacity anode material: a first-principles study. *J Mater Chem*. 2016;4:6029–6035.
209. Zhu J, Chroneos A, Eppinger J, Schwingenschlögl U. S-functionalized MXenes as electrode materials for Li-ion batteries. *Appl Mater Today*. 2016;5:19–24.
210. Wu H, Guo Z, Zhou J, Sun Z. Vacancy-mediated lithium adsorption and diffusion on MXene. *Appl Surf Sci*. 2019;488:578–585.
211. Sun F, Wang Y, Ji L, et al. Improved performances of Cr_2N monolayer as electrode of lithium ion battery through surface termination: a first-principles calculation. *J Phys Chem Solid*. 2022;168, 110794.
212. Yu Y, Guo Z, Peng Q, et al. Novel two-dimensional molybdenum carbides as high capacity anodes for lithium/sodium-ion batteries. *J Mater Chem*. 2019;7:12145–12153.
213. Kirklin S, Meredig B, Wolverton C. High-throughput computational screening of new Li-ion battery anode materials. *Adv Energy Mater*. 2013;3:252–262.
214. Li W, Li X, Liao J, et al. A new family of cation-disordered Zn (Cu)–Si–P compounds as high-performance anodes for next-generation Li-ion batteries. *Energy Environ Sci*. 2019;12:2286–2297.
215. Li W, Shen P, Yang L, et al. Novel Cu (Zn)–Ge–P compounds as advanced anode materials for Li-ion batteries. *Energy Environ Sci*. 2021;14:2394–2407.
216. Hu Z, Liu Q, Lai W, et al. Manipulating molecular structure and morphology to invoke high-performance sodium storage of copper phosphide. *Adv Energy Mater*. 2020;10, 1903542.
217. Harper AF, Evans ML, Morris AJ. Computational investigation of copper phosphides as conversion anodes for lithium-ion batteries. *Chem Mater*. 2020;32:6629–6639.
218. Bichat M-P, Politova T, Pfeiffer H, et al. Cu_3P as anode material for lithium ion battery: powder morphology and electrochemical performances. *J Power Sources*. 2004;136:80–87.
219. Li W, Li X, Yu J, et al. A self-healing layered GeP anode for high-performance Li-ion batteries enabled by low formation energy. *Nano Energy*. 2019;61:594–603.
220. Wang D-W, Zeng Q, Zhou G, et al. Carbon-sulfur composites for Li-S batteries: status and prospects. *J Mater Chem*. 2013;1:9382–9394.
221. Kaiser MR, Ma Z, Wang X, et al. Reverse microemulsion synthesis of sulfur/graphene composite for lithium/sulfur batteries. *ACS Nano*. 2017;11:9048–9056.
222. Yin L-C, Liang J, Zhou G-M, et al. Understanding the interactions between lithium polysulfides and N-doped graphene using density functional theory calculations. *Nano Energy*. 2016;25:203–210.
223. Gong Y, Ma W, Xu Z, Wang Y. Understanding the interaction of N-doped graphene and sulfur compounds in a lithium-sulfur battery-a density functional theory investigation. *New J Chem*. 2022;46, 12300.
224. Zhang Q, Wang Y, Seh ZW, et al. Understanding the anchoring effect of two-dimensional layered materials for lithium-sulfur batteries. *Nano Lett*. 2015;15:3780–3786.
225. Yi GS, Sim ES, Chung Y-C. Effect of lithium-trapping on nitrogen-doped graphene as an anchoring material for lithium-sulfur batteries: a density functional theory study. *Phys Chem Chem Phys*. 2017;19:28189–28194.
226. Wasalathilake KC, Roknuzzaman M, Ostrikov KK, et al. Interaction between functionalized graphene and sulfur compounds in a lithium-sulfur battery-a density functional theory investigation. *RSC Adv*. 2018;8:2271–2279.
227. Hou TZ, Chen X, Peng HJ, et al. Design principles for heteroatom-doped nanocarbon to achieve strong anchoring of polysulfides for lithium-sulfur batteries. *Small*. 2016;12:3283–3291.
228. Li F, Su Y, Zhao J. Shuttle inhibition by chemical adsorption of lithium polysulfides in B and N co-doped graphene for Li-S batteries. *Phys Chem Chem Phys*. 2016;18:25241–25248.
229. Zhang L, Liang P, Man X-L, et al. Fe, N co-doped graphene as a multi-functional anchor material for lithium-sulfur battery. *J Phys Chem Solid*. 2019;126:280–286.
230. Andritsos EI, Lekakou C, Cai Q. Single-atom catalysts as promising cathode materials for lithium-sulfur batteries. *J Phys Chem C*. 2021;125:18108–18118.
231. Zhang L, Liang P, Shu HB, et al. Design rules of heteroatom-doped graphene to achieve high performance lithium-sulfur batteries: both strong anchoring and catalysing based on first principles calculation. *J Colloid Interface Sci*. 2018;529:426–431.
232. Zhou G, Zhao S, Wang T, et al. Theoretical calculation guided design of single-atom catalysts toward fast kinetic and long-life Li-S batteries. *Nano Lett*. 2019;20:1252–1261.
233. Yi Z, Su F, Dai L, et al. Uncovering electrocatalytic conversion mechanisms from Li_2S_2 to Li_2S: generalization of computational hydrogen electrode. *Energy Storage Mater*. 2022;47:327–335.
234. Zeng Z, Nong W, Li Y, Wang C. Universal-descriptors-guided design of single atom catalysts toward oxidation of Li_2S in lithium-sulfur batteries. *Adv Sci*. 2021;8, 2102809.
235. Jand SP, Chen Y, Kaghazchi P. Comparative theoretical study of adsorption of lithium polysulfides (Li_2S_x) on pristine and defective graphene. *J Power Sources*. 2016;308:166–171.
236. Muhammad I, Younis U, Xie H, et al. Graphdiyne-based monolayers as promising anchoring materials for lithium-sulfur batteries: a theoretical study. *Adv. Theory. Simul.* 2020;3, 1900236.
237. Rao D, Liu X, Yang H, et al. Interfacial competition between a borophene-based cathode and electrolyte for the multiple-sulfide immobilization of a lithium sulfur battery. *J Mater Chem*. 2019;7:7092–7098.
238. Zhang Q, Xiao Y, Fu Y, et al. Theoretical prediction of B/Al-doped black phosphorus as potential cathode material in lithium-sulfur batteries. *Appl Surf Sci*. 2020;512, 145639.
239. Zhang L, Liang P, Shu H, et al. Borophene as efficient sulfur hosts for lithium-sulfur batteries: suppressing shuttle effect and improving conductivity. *J Phys Chem C*. 2017;121:15549–15555.
240. Jiang HR, Shyy W, Liu M, et al. Borophene and defective borophene as potential anchoring materials for lithium-sulfur batteries: a first-principles study. *J Mater Chem*. 2018;6:2107–2114.
241. Zhang C, He Q, Chu W, Zhao Y. Transition metals doped borophene-graphene heterostructure for robust polysulfide anchoring: a first principle study. *Appl Surf Sci*. 2020;534, 147575.

242. Zhao J, Yang Y, Katiyar RS, Chen Z. Phosphorene as a promising anchoring material for lithium-sulfur batteries: a computational study. *J Mater Chem*. 2016;4:6124–6130.
243. Mukherjee S, Kavalsky L, Chattopadhyay K, Singh CV. Adsorption and diffusion of lithium polysulfides over blue phosphorene for Li-S batteries. *Nanoscale*. 2018;10:21335–21352.
244. Lin H, Yang D-D, Lou N, et al. Defect engineering of black phosphorene towards an enhanced polysulfide host and catalyst for lithium-sulfur batteries: a first principles study. *J Appl Phys*. 2019;125, 094303.
245. Haseeb HH, Li Y, Ayub S, et al. Defective phosphorene as a promising anchoring material for lithium-sulfur batteries. *J Phys Chem C*. 2020;124:2739–2746.
246. Gong N, Hu X, Fang T, et al. Transition metals embedded siloxene as single-atom catalyst for advanced sulfur host in lithium-sulfur batteries: a theoretical study. *Adv Energy Mater*. 2022;12, 2201530.
247. Lv X, Wei W, Yang H, et al. Group IV monochalcogenides MX (M= Ge, Sn; X= S, Se) as chemical anchors of polysulfides for lithium-sulfur batteries. *Chem–Eur J*. 2018;24:11193–11199.
248. Chen X, Peng H-J, Zhang R, et al. An analogous periodic law for strong anchoring of polysulfides on polar hosts in lithium sulfur batteries: S-or Li-binding on first-row transition-metal sulfides? *ACS Energy Lett*. 2017;2:795–801.
249. Fang Q, Fang M, Liu X, et al. An asymmetric Ti_2CO/WS_2 heterostructure as a promising anchoring material for lithium-sulfur batteries. *J Mater Chem*. 2020;8:13770–13775.
250. Zhang H, Wang Z, Ren J, et al. Ultra-fast and accurate binding energy prediction of shuttle effect-suppressive sulfur hosts for lithium-sulfur batteries using machine learning. *Energy Storage Mater*. 2021;35:88–98.
251. Zhu T, Hao X, Wu Q, Wang W. Exploring anchoring performance of defective MgO nanotubes for lithium-sulphur batteries: a density functional theory (DFT) study. *Can J Chem Eng*. 2022;100:979–989.
252. Wang D, Li F, Lian R, et al. A general atomic surface modification strategy for improving anchoring and electrocatalysis behavior of $Ti_3C_2T_2$ MXene in lithium-sulfur batteries. *ACS Nano*. 2019;13:11078–11086.
253. Xiao Z, Li Z, Meng X, Wang R. MXene-engineered lithium-sulfur batteries. *J Mater Chem*. 2019;7:22730–22743.
254. Zhang C, Cui L, Abdolhosseinzadeh S, Heier J. Two-dimensional MXenes for lithium-sulfur batteries. *InfoMat*. 2020;2:613–638.
255. Liang X, Garsuch A, Nazar LF. Sulfur cathodes based on conductive MXene nanosheets for high-performance lithium-sulfur batteries. *Angew Chem Int Ed Engl*. 2015;54:3907–3911.
256. Sim ES, Yi GS, Je M, et al. Understanding the anchoring behavior of titanium carbide-based MXenes depending on the functional group in Li-S batteries: a density functional theory study. *J Power Sources*. 2017;342:64–69.
257. Rao D, Zhang L, Wang Y, et al. Mechanism on the improved performance of lithium sulfur batteries with MXene-based additives. *J Phys Chem C*. 2017;121:11047–11054.
258. Zhao Y, Zhao J. Functional group-dependent anchoring effect of titanium carbide-based MXenes for lithium-sulfur batteries: a computational study. *Appl Surf Sci*. 2017;412:591–598.
259. Liu X, Shao X, Li F, Zhao M. Anchoring effects of S-terminated Ti_2C MXene for lithium-sulfur batteries: a first-principles study. *Appl Surf Sci*. 2018;455:522–526.
260. Li N, Meng Q, Zhu X, et al. Lattice constant-dependent anchoring effect of MXenes for lithium-sulfur (Li-S) batteries: a DFT study. *Nanoscale*. 2019;11:8485–8493.
261. Wang Y, Shen J, Xu LC, et al. Sulfur-functionalized vanadium carbide MXene (V2CS2) as a promising anchoring material for lithium-sulfur batteries. *Phys Chem Chem Phys*. 2019;21:18559–18568.
262. Li F, Zhang X, Liu X, Zhao M. Novel conductive metal-organic framework for a high-performance lithium-sulfur battery host: 2D Cu-benzenehexathial (BHT). *ACS Appl Mater Interfaces*. 2018;10:15012–15020.
263. Song X, Qu Y, Zhao L, Zhao M. Monolayer Fe_3GeX_2 (X= S, Se, and Te) as highly efficient electrocatalysts for lithium-sulfur batteries. *ACS Appl Mater Interfaces*. 2021;13:11845–11851.
264. Gao W, Chen Y, Li B, et al. Determining the adsorption energies of small molecules with the intrinsic properties of adsorbates and substrates. *Nat Commun*. 2020;11:1196.
265. Larcher D, Tarascon J-M. Towards greener and more sustainable batteries for electrical energy storage. *Nat Chem*. 2015;7:19–29.
266. Zhang H, Gao Y, Chen M, et al. Organic small molecules with electrochemical-active phenolic enolate groups for ready-to-charge organic sodium-ion batteries. *Small Methods*. 2022;6, 2200455.

Ke Fan received her Ph.D. from The Hong Kong Polytechnic University. Currently, she is a postdoctoral fellow in the Department of Applied Physics, The Hong Kong Polytechnic University, under the supervision of Prof. Haitao Huang and Dr. Yuen Hong Tsang. Her research interests include computational design of low-dimensional materials for metal-ion and metal-sulfur batteries.

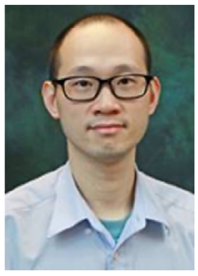

Yuen Hong Tsang is an associate professor in the Department of Applied Physics and Photonics Research Institute, The Hong Kong Polytechnic University. His current research interests include renewable energy, solar energy conversion, laser development, and novel materials for photonic and electronic devices.

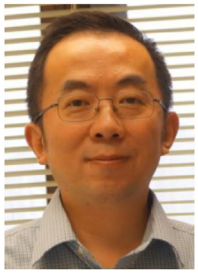

Haitao Huang is a professor in the Department of Applied Physics and Research Institute for Smart Energy, The Hong Kong Polytechnic University. His current research interests include electrochemical energy storage and conversion, and ferroelectric materials for energy applications. He is currently the board committee member of the International Academy of Electrochemical Energy Science (IAOEES) and the fellow of the Royal Society of Chemistry.